# Moment-of-Fluid Analytic Reconstruction on 3D Rectangular Hexahedrons

Thomas Milcent[a], Antoine Lemoine[b]

[a]*Arts et Métiers ParisTech, I2M, UMR 5295, F-33400 Talence, France.*
[b]*Bordeaux INP, I2M, UMR 5295, F-33400 Talence, France.*

**Abstract**

The moment-of-fluid method (MOF) is a second-order accurate interface reconstruction method which can be seen as an extension of the volume-of-fluid method with piecewise linear interface construction (VOF-PLIC). MOF involves a computationally intensive minimization problem that needs to be solved on every cell containing several materials. We propose a new fast and robust reconstruction algorithm to tackle this problem on rectangular hexahedral cells. Our approach uses explicit analytic formulas of the objective function that does not use any geometric computations such as half-space–polyhedron intersections. The numerical results show that the proposed method is more robust and more than 100 times faster than the original approach. Additionally, we propose a faster reconstruction algorithm on convex polyhedral cells. All the methods presented in this article have been implemented and verified on the open-source code Notus.

*Keywords:* Moment-of-Fluid, interface reconstruction, material tracking, PLIC, centroid locus

## 1. Introduction

Common engineering problems involve several materials interacting with each other. The numerical simulations of these phenomena require the tracking of the location of the materials over time. Across the interface between two materials, some physical phenomena must be described such as the heat or mass transfer. Any numerical errors on the location of the interface have an impact on the physics of the whole problem. As a result, the numerical simulations require accurate tracking methods. In this article we only consider numerical methods designed for the Eulerian framework where the velocity field is defined on the whole domain and where the motion of the materials is independent of the underlying mesh.

A lot numerical strategies have been developed to track the materials in this context such as the level-set method [1], the front-tracking method [2], and the volume-of-fluid method with piecewise linear interface construction (VOF-PLIC). For the latter, any cell containing two materials is partitioned by a linear interface such that the volume of each part contains exactly the same volume as the real location of the material. The most common application of the VOF-PLIC method is the advection of the materials which is composed of two steps. In the first step, the geometry of the partition is advected with a Lagrangian method, and then the volume of each material is computed from the intersection of the geometry with the underlying mesh. In the second step, named *reconstruction*, a new partition is computed using the volume in each cells and their neighborhood.

Recently the moment-of-fluid method (MOF) [3–22] was introduced as a second-order accurate extension of the VOF-PLIC method for multi-material reconstruction. Besides the volume of the materials, MOF involves the centroids of each material which allows to reconstruct the partition with only the information contained in the cell. Furthermore, this method offers a straightforward way to represent $n \geq 2$ materials in the same cell [5, 6]. The improved accuracy of this method is at the expense of the time to partition the cell which involves a computationally intensive minimization problem. In this article, we present a fast and

---

robust reconstruction strategy to solve this minimization problem on rectangular hexahedrons. Note that we only address the problem of the reconstruction, the advection can be done, for instance, using a Lagrangian remapping method [4] or a directional splitting method [12].

The currently proposed method falls under the continuity of the improvements made to MOF during the past decade. MOF was originally introduced in 2D on polygonal cells [3, 4]. It was quickly extended to multi-material reconstruction in 3D by Ahn & Shashkov [5] and in 2D by Dyadechko & Shashkov [6]. Note that the latter defines a convenient error criterion and provides a convergence study of the MOF reconstruction. Another effort to extend MOF to any coordinate system was made by Anbarlooei & Mazaheri [8] who have extended MOF to axisymmetric meshes. As MOF is a PLIC method, it is vulnerable to filaments that can not be advected. Jemison *et al.* [16] solved this problem by adapting MOF to filament capturing which can be done in a straightforward way by using a $n$-material reconstruction and allowing two materials to be identical in one cell. To improve the robustness of MOF, many solutions were proposed, such as the one advanced by Hill & Shashkov [13] which consists in changing slightly the minimization problem of MOF to minimize the centroid difference on both the material and its complementary. Since the objective function of MOF contains local minima where the minimization algorithms are prone to fall into, Qing *et al.* [22] have proposed a method in 2D that finds all the minima of the MOF problem and selects the best one. This gain of robustness is at the expense of the runtime of the algorithm.

MOF was designed to be used in conjunction with other methods. Ahn & Shashkov [7] proposed an interaction of MOF with an adaptive mesh refinement (AMR) strategy where the centroid difference is used as a criterion for mesh refinement. The coupling with an Arbitrary Lagrangian-Eulerian (ALE) strategy is also found among many authors [9, 11, 14]. Valuable implementation details can be found in many publications, for instance, in [10] MOF was coupled with a code based on the finite element method (FEM) and in [15] MOF is used in a compressible context. In [12] and [21], MOF is coupled with the levelset method (CLSMOF) and more recently, Kikinzon *et al.* [20] proposed a data structure to represent the partition of the multi-material reconstruction to simplify the interaction with other methods.

The most expensive part of the MOF reconstruction is the evaluation of the objective function and its partial derivatives at each iteration of the minimization algorithm which involves computationally intensive geometrical manipulations. To tackle this problem, Chen & Zhang proposed analytic formulas for the partial derivatives of the objective function on convex polyhedral cells [17] and convex polygonal cells [19]. However, their methods requires a prior evaluation of the objective function with a geometric approach that still remains expensive. To completely avoid these computationally intensive geometric manipulations, another approach is to express the objective function with analytic formulas. This has been addressed by Lemoine *et al.* [18] in 2D for rectangular cells as we will discuss in section 2.3. In this paper, we propose a 3D extension of this method to rectangular hexahedral cells. This method can be applied to geometry tracking on any meshes composed of this kind of cells such as rectilinear grids with or without AMR.

## 2. The moment-of-fluid method

### 2.1. The moment-of-fluid problem

The MOF problem can be summarized as follows. Consider $\Omega \subset \mathbb{R}^3$ a portion of space, for instance a polyhedral cell and $M \subset \Omega$ the location of a given material in $\Omega$, as depicted on the left of figure 1. Where the VOF-PLIC method requires the information of the volume of material from the cell and its neighborhood, MOF embeds all the information within the cell. Besides the volume of material, the MOF reconstruction involves the centroid of M denoted by $\mathcal{C}(M)$ and defined by:

$$\mathcal{C}(M) = \frac{1}{\text{vol}(M)} \int_M \boldsymbol{x} \mathrm{d}\boldsymbol{x} \tag{1}$$

As a PLIC method, MOF approximates the location of the material M with a linear interface between the materials in $\Omega$. The resulting volume is the intersection of a half-space with $\Omega$. A half-space can be defined by two parameters, namely the outgoing unit normal $\boldsymbol{n}$ of its boundary and the shortest signed distance $d$ of its boundary to the origin. We denote $\mathrm{H}(\boldsymbol{n}, d) = \left\{ \boldsymbol{x} \in \mathbb{R}^3 \mid \boldsymbol{x} \cdot \boldsymbol{n} \leq d \right\}$ a half-space parametrized by $\boldsymbol{n}$

and $d$. As a result, the approximation of M is equal to $\mathrm{H}(\boldsymbol{n}, d) \cap \Omega$ (right of figure 1) with $\boldsymbol{n}$ and $d$ to be determined. Like the VOF methods, MOF enforces the volume conservation on its reconstruction, that is $\mathrm{vol}(\mathrm{H}(\boldsymbol{n}, d) \cap \Omega) = \mathrm{vol}(\mathrm{M})$. In summary, the set of all the approximations of M in $\Omega$ can be defined by:

$$\mathfrak{A} = \left\{ \mathrm{H}(\boldsymbol{n}, d) \cap \Omega \mid \boldsymbol{n} \in \mathbb{S}^2, d \in \mathbb{R} \text{ and } \mathrm{vol}\big(\mathrm{H}(\boldsymbol{n}, d) \cap \Omega\big) = \mathrm{vol}(\mathrm{M}) \right\} \tag{2}$$

The moment-of-fluid problem consists in finding the best approximation $\omega^* \in \mathfrak{A}$ of M such that its centroid is as close as possible to the centroid of the real — or *reference* — material location M denoted by $\mathcal{C}^\star = \mathcal{C}(\mathrm{M})$. Written in mathematical terms, the MOF problem becomes:

$$\text{Find } \omega^* \in \mathfrak{A} \text{ such that } \quad \omega^* = \operatorname*{argmin}_{\omega \in \mathfrak{A}} \big|\mathcal{C}(\omega) - \mathcal{C}^\star\big|^2 \tag{3}$$

Note that the solution may be not unique, but as proved in [3], the set of reference centroids for which the problem is non-unique has zero area.
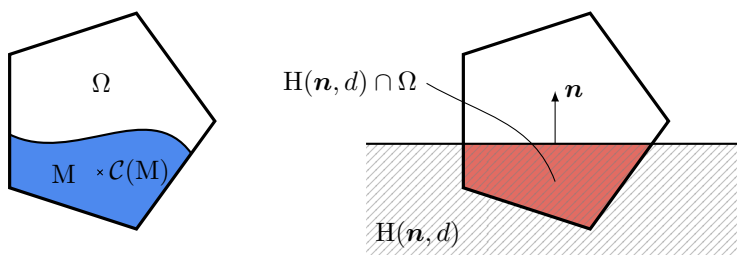


Figure 1: Illustration of the notations used to define the MOF problem.

## 2.2. General method to solve the moment-of-fluid problem

To solve the MOF problem (3), various iterative minimization algorithms have been proposed. For instance, Ahn & Shashkov [5] use a Broyden-Fletcher-Goldfarb-Shanno (BFGS) algorithm, while other authors, such as Jemison *et al.* [12], prefer a Gauss-Newton method. The minimization algorithms require several evaluations of the objective function and its partial derivatives. The evaluation of the objective function requires to compute the centroid of the approximation $\mathcal{C}(\omega)$ and, therefore, the approximation $\omega$ itself. From (2), each approximation $\omega$ is defined by a direction $\boldsymbol{n}$ and a distance $d$. In practice, each step of the minimization algorithm provides a new direction $\boldsymbol{n}$ and the distance $d$ is determined using a volume enforcement algorithm. Following Dyadechko & Shashkov [4], such an algorithm will be referred to as a *flood algorithm*. It consists to find the distance $d$ of a half-space such that the volume of the intersection of this half-space and the cell is exactly equal to the prescribed volume. For instance, there is the Brent's-based method [23] or the more recent algorithm proposed by Diot & François [24] in 2016. All these algorithms involve to compute the intersection of a plane and a polyhedron which makes this algorithm computationally intensive.

The classic strategy to evaluate the partial derivatives consists to use a finite-difference scheme. With a centered scheme, two computations of the centroid are required per direction which makes a total of four calls to the flood algorithm in 3D. Dyadechko & Shashkov [3] proposed a formula to compute the derivative of the objective function on 2D polygonal cells using the prior evaluation of the objective function. This formula reduces the number of reconstructions to only one per evaluation of the objective function and its partial derivatives. Furthermore, this formula gives an exact value where the finite-difference scheme only gives an approximation. In [19], Chen & Zhang proposed a proof of this formula and, in a second article [17], they have derived some formulas for 3D to compute the partial derivatives on convex polyhedral cells that are summarized in Appendix A.

Another approach to solve the MOF problem (3) consists to express the objective function with analytic formulas. This can be done by finding the locus of the centroids $\mathcal{C}(\omega(\boldsymbol{n}))$ for a given fixed volume and for all the normals $\boldsymbol{n}$. This locus is a closed curve in 2D and a closed surface in 3D. Finding a parametrization of this locus is a very difficult task on general polygonal or polyhedral cells. However, on rectangular cells, this approach has been successfully applied for the first time by Lemoine *et. al* [18] as presented below.

## 2.3. Analytic method to solve the moment-of-fluid problem in 2D on rectangular cells

Consider a rectangular cell $\Omega = [0, c_1] \times [0, c_2]$. In [18], Lemoine *et al.* proved that the locus of the centroids is the reunion of 4 arcs of parabolas and 4 arcs of hyperbolas as depicted in figure 2. To find a global parametrization of the locus of the centroid, we introduce the angle $\theta$ defined such that the normal verifies $\boldsymbol{n}(\theta) = [\cos(\theta), \sin(\theta)]$ and we denote by $\mathcal{C}^{\mathcal{V}}(\theta)$ the centroid of the approximation $\mathcal{C}(\omega(\boldsymbol{n}(\theta)))$. The MOF problem (3) can be reinterpreted as finding the angle $\theta^*$ such that:

$$\theta^* = \underset{\theta \in [0, 2\pi]}{\operatorname{argmin}} \left| \mathcal{C}^{\mathcal{V}}(\theta) - \mathcal{C}^{\star} \right|^2 \tag{4}$$

Taking the derivative of the objective function in (4), the minimum verifies the following relation where $\boldsymbol{u} \cdot \boldsymbol{v}$ denotes the dot product between two vectors $\boldsymbol{u}$ and $\boldsymbol{v}$:

$$\left( \mathcal{C}^{\mathcal{V}}(\theta^*) - \mathcal{C}^{\star} \right) \cdot \partial_\theta \mathcal{C}^{\mathcal{V}}(\theta^*) = 0 \tag{5}$$

It is shown that this equation is a third degree polynomial for the parabola or a fourth degree polynomial for the hyperbola. Remark that beyond finding a parametrization of the locus of the centroid, this method gives a fully analytic solution of the MOF problem.
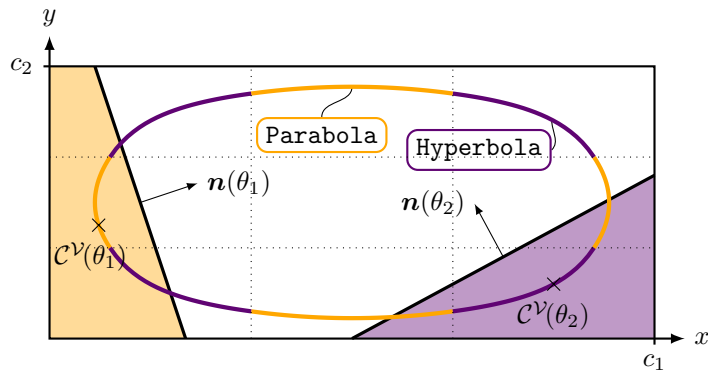


Figure 2: Illustration of the locus of the centroids (the curve) on rectangular cells for a fixed volume $\mathcal{V}$. The curve is composed of 4 arcs of parabolas and 4 arcs of hyperbola. The yellow region corresponds to an approximation shaped as a quadrangle. Its centroid is on a parabola. The purple region corresponds to an approximation shaped as a triangle. Its centroid is on a hyperbola. The purple and the yellow regions share the same area.

In this article, we have applied this methodology in 3D to rectangular hexahedrons. We will see that instead of two different configurations — triangle and quadrangle — there are five different configurations. The solution of the MOF problem verifies equation (8) which is the 3D equivalent of equation (5). In two of the five configurations, this equation reduces to two polynomial equations of fifth and twelfth degree without trivial roots, and because of the Abel–Ruffini theorem there are no general algebraic formulas to express these roots. Furthermore, in the three remaining configurations, the solution cannot be expressed as a root of a polynomial. Therefore, there is no fully analytical solution of the MOF problem (3) on rectangular hexahedron. Instead, we use a minimization algorithm where the objective function and its partial derivatives are expressed as a set of analytic formulas.

The remainder of this article is organized as follows. Section 3 describes our method as a black-box to compute the centroid and the partial derivatives for a given normal $\boldsymbol{n}$. The proof of these formulas are given in Appendix C. Section 4 presents a set of numerical tests to measure the efficiency and the robustness of our method compared to three geometric approaches. Two of them are detailed in Appendix A and Appendix B. Section 5 presents the conclusions and the future work.

4

## 3. Analytic method on rectangular hexahedrons

### 3.1. Description

In the remainder of this article, we consider a rectangular hexahedron $\Omega = [0, c_1] \times [0, c_2] \times [0, c_3]$. Recall that MOF consists in finding the best approximation of the material location $M \subset \Omega$. We define $\mathcal{V} = \text{vol}(M)$ as the volume of M — or *reference volume* — and $\mathcal{C}^\star$ as its centroid. From the definition of the set of the approximations $\mathfrak{A}$ in equation (2), any element of this set shares the same volume $\mathcal{V}$ as the material location M. We introduce in the following equation the normal $\boldsymbol{n}(\theta, \phi)$ of the half-space parametrized by the spherical coordinates $\theta$ and $\phi$.

$$\boldsymbol{n}(\theta, \phi) = \begin{bmatrix} \sin(\phi)\cos(\theta) \\ \sin(\phi)\sin(\theta) \\ \cos(\phi) \end{bmatrix} \tag{6}$$

Consider an approximation $\omega(\boldsymbol{n}) \in \mathfrak{A}$ generated by the direction $\boldsymbol{n}$ as defined in section 2. We denote $\mathcal{C}^\mathcal{V}(\theta, \phi)$ the centroid of the approximation $\mathcal{C}(\omega(\boldsymbol{n}(\theta, \phi)))$. In equation (7), we define the objective function of the minimization problem (3) using the spherical coordinates.

$$\mathcal{F}(\theta, \phi) = \left| \mathcal{C}^\mathcal{V}(\theta, \phi) - \mathcal{C}^\star \right|^2 \tag{7}$$

The minimization algorithm requires to evaluate the objective function (7) and its partial derivatives given by the following formulas:

$$\partial_\theta \mathcal{F}(\theta, \phi) = 2\big(\mathcal{C}^\mathcal{V}(\theta, \phi) - \mathcal{C}^\star\big) \cdot \partial_\theta \mathcal{C}^\mathcal{V}(\theta, \phi) \qquad \partial_\phi \mathcal{F}(\theta, \phi) = 2\big(\mathcal{C}^\mathcal{V}(\theta, \phi) - \mathcal{C}^\star\big) \cdot \partial_\phi \mathcal{C}^\mathcal{V}(\theta, \phi) \tag{8}$$

Our method consists in finding a global parametrization of the locus of the centroids $(\theta, \phi) \mapsto \mathcal{C}^\mathcal{V}(\theta, \phi)$ denoted by $\mathfrak{L}^\mathcal{V}$ and defined in the following equation:

$$\mathfrak{L}^\mathcal{V} = \big\{ \mathcal{C}^\mathcal{V}(\theta, \phi) \ \big| \ \theta \in [-\pi, \pi] \text{ and } \phi \in [0, \pi] \big\} \tag{9}$$

To simplify the problem, we assume that the reference volume $\mathcal{V}$ is less than half of the volume of the cell: $\mathcal{V} \leq \text{vol}(\Omega)/2$. The case where $\mathcal{V} > \text{vol}(\Omega)/2$ can be treated by considering the complementary $\Omega \setminus M$. In the remainder of this article, we will refer to the volume fraction $\chi = \mathcal{V}/\text{vol}(\Omega)$ as the ratio between the reference volume and the volume of the hexahedron.
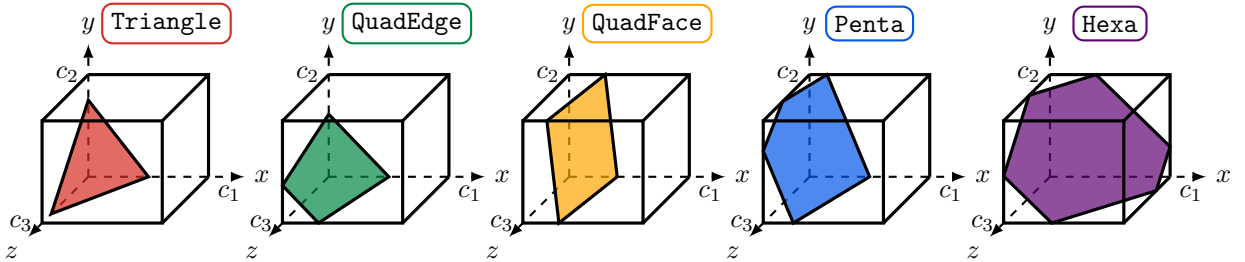


Figure 3: Five ways to intersect a rectangular hexahedron with a half-space: `Triangle`, `QuadEdge`, `QuadFace`, `Penta` and `Hexa`.

The shape of the locus of the centroids depends on how the half-space intersects the hexahedron, and as shown in figure 3, a half-space can intersect a hexahedron in five different ways. We denote `Triangle`, `QuadEdge`, `QuadFace`, `Penta` and `Hexa` the five possible configurations. We define $\mathfrak{P}$ the surface defined as the intersection of the boundary of the half-space and the hexahedron $\Omega$.

$$\mathfrak{P} = \big\{ \boldsymbol{x} \in \Omega \ \big| \ \boldsymbol{x} \cdot \boldsymbol{n} = d \big\} \tag{10}$$

In the `Triangle` configuration, which exists if $\chi < \frac{1}{6}$, the half-space contains one vertex of the hexahedron and the surface $\mathfrak{P}$ is a triangle. In the `QuadEdge` configuration, the half-space contains one edge of the

5

hexahedron and the surface is a quadrangle. In the `QuadFace` configuration, the half-space contains one face of the hexahedron and the surface is also a quadrangle. In the `Penta` configuration, the half-space contains two edges of the hexahedron and the surface $\mathfrak{P}$ is a pentagon. In the `Hexa` configuration, which exists if $\chi > \frac{1}{6}$, the half-space contains three edges of the hexahedron and the surface $\mathfrak{P}$ is a hexagon. Overall, the locus of the centroids is the combination of 50 configurations composed of 8 `Triangle` or `Hexa` (one per vertex), 6 `QuadFace` (one per face), 12 `QuadEdge` (one per edge) and 24 `Penta` (four per face). In the remainder of this article, we use the same colors as in figure 3 to depict all the configurations (refer to the web version of this article to see the colors).

Figure 4 depicts the locus of the centroids $\mathfrak{L}^{\mathcal{V}}$ for $\chi = 0.1$ (left) and $\chi = 0.4$ (right) where the dimensions of the hexahedron are $(c_1, c_2, c_3) = (1, 3, 2)$. We observe that the `Triangle` surface is only present on the locus of the left, whereas the `Hexa` surface is present on the locus of the right. When $\chi = \frac{1}{6}$, there are no `Triangle` or `Hexa` surfaces. The shape of the `QuadEdge` and `Penta` surfaces also depends on the volume fraction. When $\chi < \frac{1}{6}$, the boundary of the `QuadEdge` surface is composed of 6 curves and the boundary of the `Penta` surface is composed of 3 curves, while when $\chi > \frac{1}{6}$, the boundary of the `QuadEdge` surface is composed of 4 curves and the boundary of the `Penta` surface is composed of 4 curves. In the extreme case, when $\chi = \frac{1}{2}$, the `QuadFace` and the `Hexa` surfaces are the only surfaces that remain on the locus of the centroids.

In the remainder of this section, we give a parametrization of the surface $\mathfrak{L}^{\mathcal{V}}$ in terms of the spherical coordinates $(\theta, \phi)$. There is no point to provide the equations of the 50 pieces of the surface, since only 4 are sufficient to describe the whole surface (remember that the `Triangle` and the `Hexa` configurations are mutually exclusives). The symmetry of the hexahedron allows to describe the other pieces by rotations or reflections of the hexahedron, and some permutations of $(c_1, c_2, c_3)$.
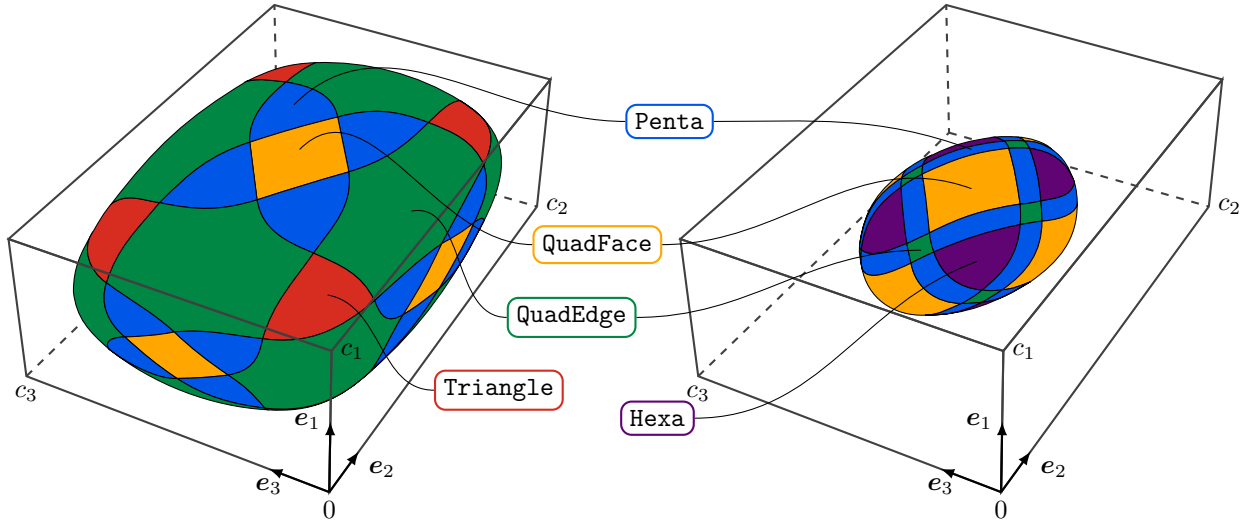


Figure 4: Locus of the centroids for the volume fractions $\chi = 0.1$ (left) and $\chi = 0.4$ (right). The dimensions of the hexahedron are $c_1 = 1$, $c_2 = 3$ and $c_3 = 2$.

### 3.2. Parametrization of the locus of the centroids in the reference chart

The number of configurations can be reduced by remarking that the locus of the centroids is symmetric about the three planes $\{x = c_1/2\}$, $\{y = c_2/2\}$ and $\{z = c_3/2\}$. Thus, we choose to reduce the *global chart* $[-\pi, \pi] \times [0, \pi]$ to the region $[0, \pi/2]^2$, referred to as *local chart*, as depicted in figure 5. The consequence of using the definition (6) for the normal to the half-space is that the basis of the Cartesian coordinates $(\boldsymbol{e_1}, \boldsymbol{e_2}, \boldsymbol{e_3})$ corresponds to $\boldsymbol{e_1} = \boldsymbol{n}(0, \pi/2)$, $\boldsymbol{e_2} = \boldsymbol{n}(\pi/2, \pi/2)$, and $\boldsymbol{e_3} = \boldsymbol{n}(\theta, 0)$. In terms of surface, the considered region corresponds to the part of the locus $\mathfrak{L}^{\mathcal{V}}$ such that $x_i \in [0, c_i/2]$ for $i \in \{1, 2, 3\}$. Note that the origin of the coordinates corresponds to one of the vertices of the hexahedron as depicted in figure 4.

6

Figure 5 represents the local charts in $\theta$ and $\phi$ corresponding to the locus of the centroids for the volume fractions $\chi = 0.1$ (left) and $\chi = 0.25$ (right). With this parametrization, the distances and the areas of the configurations are highly distorted when $\phi$ approaches 0. At the limit, the line $\phi = 0$ maps to a single point which corresponds to the south pole of the locus (remember that the centroid is inside the half-space, in the opposite direction of the normal like in 2D as depicted in figure 2). In these local charts, 10 pieces are still involved in the description of the locus $\mathfrak{L}^{\mathcal{V}}$. As shown in figure 5, the *reference chart* is defined as the region enclosed by a bold line which contains exactly one `Penta`, one `QuadEdge`, one `QuadFace` and one `Triangle` (or `Hexa` if $\chi > \frac{1}{6}$). It is delimited on the top by the line $\phi = \frac{\pi}{2}$ for $\theta \in [0, \theta_5]$ and is delimited on the left by the line $\theta = 0$ for $\phi \in [\phi_{\mathrm{p1}}^{\mathrm{lim}}(0), \frac{\pi}{2}]$. The other limits are given by the curves $\phi_\star^{\mathrm{lim}}$ defined in section 3.2.1. The dotted bold line corresponding to the limit $\phi_{\mathrm{rot}}^{\mathrm{lim}}$ will be used later in section 3.3. We will see in section 3.3.4 that any coordinates $(\theta, \phi)$ in the global chart can be transformed to the reference map by some symmetries as depicted in figure 6.
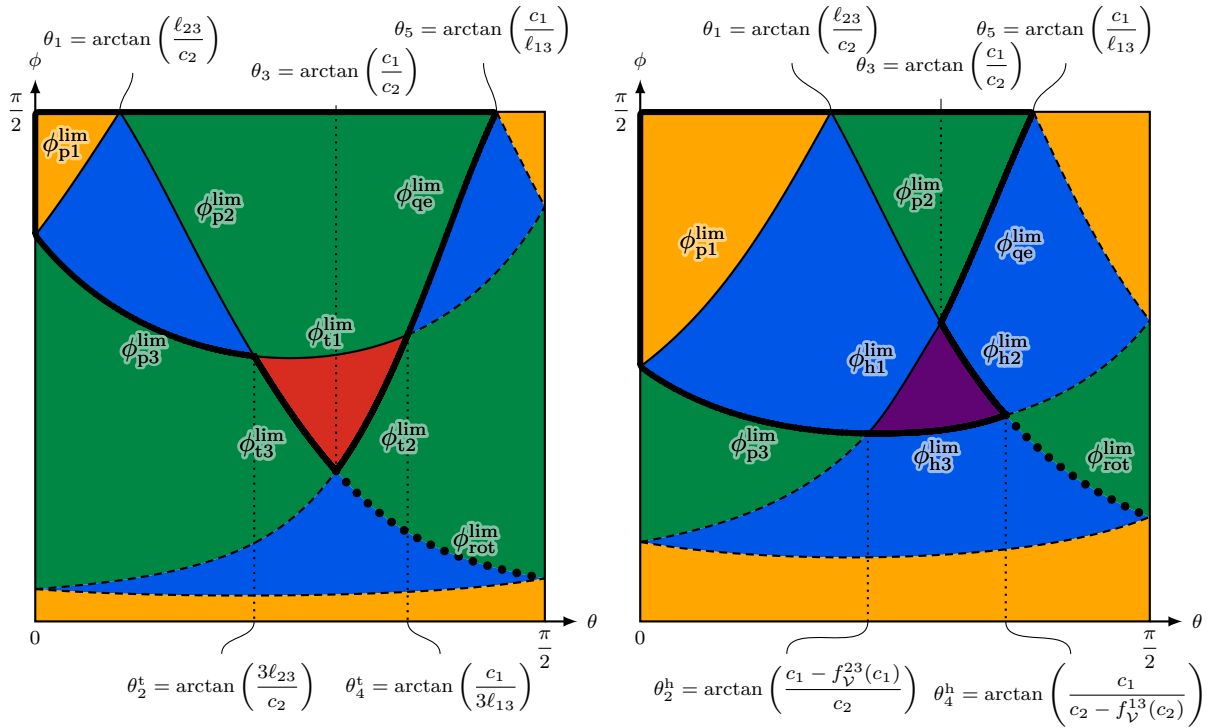


Figure 5: Local charts of the locus of the centroids reduced to $[0, \pi/2]^2$ for the volume fractions $\chi = 0.1$ (left) and $\chi = 0.25$ (right). The dimensions of the hexahedron are $c_1 = 2$, $c_2 = 1.5$ and $c_3 = 1$. The bold regions correspond to the reference chart that contains 4 configurations (`Triangle` and `Hexa` are mutually exclusive).

In the remainder of this section, we present how to compute the centroid and its partial derivatives from any point of the reference chart. First, in section 3.2.1, we present the equations of the limit curves $\phi_\star^{\mathrm{lim}}$. Then, in section 3.2.2, we present the parametrization of the centroid and its partial derivatives in the reference chart.

### 3.2.1. Limits of the reference chart

We introduce the notations in equation (11) to simplify the formulas given in this section. The proof of the formulas presented in this section is given in Appendix C.

$$\ell_{ij} = \frac{2\mathcal{V}}{c_i c_j} \quad f_{\mathcal{V}}^{ij}(x) = \frac{-x + \sqrt{12\ell_{ij}x - 3x^2}}{2} \quad T_1 = c_1 \cot(\theta) \quad T_2 = c_2 \tan(\theta) \quad T_3 = c_3 \cot(\phi)\sec(\theta) \quad (11)$$

7

In the `Triangle` configuration, the limit curves are given by equations (12). Note that $\mathrm{arccot}(x) = \frac{\pi}{2} - \arctan(x)$ when $x > 0$, which is verified in all our formulas. We recommend to use the formulas with arctan instead of arccot or check that $\mathrm{arccot}(0) = \frac{\pi}{2}$ to machine precision.

$$\phi_{\mathrm{t1}}^{\lim}(\theta) = \mathrm{arccot}\left(\sqrt{3\ell_{23}T_2}\,\frac{\cos(\theta)}{c_3}\right) \quad \phi_{\mathrm{t2}}^{\lim}(\theta) = \mathrm{arccot}\left(\frac{(T_1)^2}{3\ell_{13}}\frac{\sin(\theta)}{c_3}\right) \quad \phi_{\mathrm{t3}}^{\lim}(\theta) = \mathrm{arccot}\left(\frac{(c_2\sin(\theta))^2}{3\ell_{12}(c_1\cos(\theta))}\right) \tag{12}$$

In the `Penta` configuration, the limit curves are given by:

$$\phi_{\mathrm{p1}}^{\lim}(\theta) = \mathrm{arccot}\left((\ell_{23} - T_2)\,\frac{\cos(\theta)}{c_3}\right) \tag{13a}$$

$$\phi_{\mathrm{p2}}^{\lim}(\theta) = \mathrm{arccot}\left((T_2 - f_{\mathcal{V}}^{23}(T_2))\,\frac{\cos(\theta)}{c_3}\right) \tag{13b}$$

$$\phi_{\mathrm{p3}}^{\lim}(\theta) = \mathrm{arccot}\left(\left(\ell_{23} + T_2 + \sqrt{(\ell_{23}+T_2)^2 - \frac{4}{3}(T_2)^2}\right)\frac{\cos(\theta)}{2c_3}\right) \tag{13c}$$

The limit curve in the `QuadEdge` configuration and for the rotation (see section 3.3) are given by:

$$\phi_{\mathrm{qe}}^{\lim}(\theta) = \mathrm{arccot}\left((T_1 - f_{\mathcal{V}}^{13}(T_1))\,\frac{\sin(\theta)}{c_3}\right) \tag{14a}$$

$$\phi_{\mathrm{rot}}^{\lim}(\theta) = \mathrm{arccot}\left(\left(c_2\sin(\theta) - c_1\cos(\theta) + \frac{(c_1\cos(\theta))^2}{3c_2\sin(\theta)}\right)\frac{1}{\ell_{12}}\right) \tag{14b}$$

In the `Hexa` configuration, the limit curves are given by equations (15a), (15b), and (15c).

$$\phi_{\mathrm{h1}}^{\lim}(\theta) = \mathrm{arccot}\left(\left(c_1 - 2\sqrt{\ell_{23}T_2}\cos\left(\frac{1}{3}\arccos\left(\frac{3c_1(c_1 - \ell_{23} - T_2) + (T_2)^2}{2\ell_{23}\sqrt{\ell_{23}T_2}}\right) + \frac{4\pi}{3}\right)\right)\frac{\cos(\theta)}{c_3}\right) \tag{15a}$$

$$\phi_{\mathrm{h2}}^{\lim}(\theta) = \mathrm{arccot}\left(\left(c_2 - 2\sqrt{\ell_{13}T_1}\cos\left(\frac{1}{3}\arccos\left(\frac{3c_2(c_2 - \ell_{13} - T_1) + (T_1)^2}{2\ell_{13}\sqrt{\ell_{13}T_1}}\right) + \frac{4\pi}{3}\right)\right)\frac{\sin(\theta)}{c_3}\right) \tag{15b}$$

$$\phi_{\mathrm{h3}}^{\lim}(\theta) = \mathrm{arccot}\left(\left(c_1 + T_2 + 2\sqrt{(2c_1 - \ell_{23})T_2}\cos\left(\frac{1}{3}\arccos\left(\frac{3(c_1 - \ell_{23})(c_1 + T_2)}{2(2c_1 - \ell_{23})\sqrt{(2c_1 - \ell_{23})T_2}}\right) + \frac{4\pi}{3}\right)\right)\frac{\cos(\theta)}{c_3}\right) \tag{15c}$$

### 3.2.2. Centroids and derivatives in spherical coordinates in the reference chart

The parametrization of the centroid locus $\mathcal{C}^{\mathcal{V}}(\theta, \phi)$ is defined as a piecewise function on each configuration. Inside the reference chart, it is given by equations (16) to (20). As in section 3.2.1, the notations defined in (11) are used to simplify the formulas in this section.

In the `Triangle` configuration, the parametrization is given by equation (16) which is defined for $\chi < \frac{1}{6}$.

$$\mathcal{C}_{\mathrm{t}}^{\mathcal{V}}(\theta, \phi) = \frac{1}{4}(3\ell_{23}T_2T_3)^{1/3}\begin{bmatrix} 1 \\ c_2/T_2 \\ c_3/T_3 \end{bmatrix} \tag{16}$$

In the `QuadFace` configuration, the parametrization is given by:

$$\mathcal{C}_{\mathrm{qf}}^{\mathcal{V}}(\theta, \phi) = \frac{1}{12\ell_{23}}\begin{bmatrix} 3(\ell_{23})^2 + (T_2)^2 + (T_3)^2 \\ 2c_2(3\ell_{23} - T_2) \\ 2c_3(3\ell_{23} - T_3) \end{bmatrix} \tag{17}$$

In the `QuadEdge` configuration, the parametrization is given by:

$$\mathcal{C}_{\mathrm{qe}}^{\mathcal{V}}(\theta,\phi) = \frac{1}{108\ell_{23}} \begin{bmatrix} \frac{1}{T_2}\mathcal{F}_{\mathrm{qe}}(T_2,T_3)\mathcal{X}_{\mathrm{qe}} \\ \frac{c_2}{(T_2)^2}\mathcal{F}_{\mathrm{qe}}(T_2,T_3)\mathcal{X}_{\mathrm{qe}} \\ 3c_3\left(18\ell_{23} - \frac{T_3}{T_2}\mathcal{X}_{\mathrm{qe}}\right) \end{bmatrix} \qquad \mathcal{F}_{\mathrm{qe}}(x,y) = 6\ell_{23}x + y^2 \qquad \mathcal{X}_{\mathrm{qe}} = \sqrt{36\ell_{23}T_2 - 3(T_3)^2} \quad (18)$$

In the `Penta` configuration, the parametrization is given by:

$$\mathcal{C}_{\mathrm{p}}^{\mathcal{V}}(\theta,\phi) = \frac{1}{6\ell_{23}} \begin{bmatrix} \mathcal{F}_{\mathrm{p}}^0(T_2,T_3) + \mathcal{F}_{\mathrm{p}}^1(T_2,T_3)\mathcal{X}_{\mathrm{p}} + 24T_2T_3(\mathcal{X}_{\mathrm{p}})^2 \\ c_2\left(\mathcal{F}_{\mathrm{p}}^2(T_2,T_3) + \mathcal{F}_{\mathrm{p}}^3(T_2,T_3)\mathcal{X}_{\mathrm{p}} - 24T_3(\mathcal{X}_{\mathrm{p}})^2\right) \\ c_3\left(\mathcal{F}_{\mathrm{p}}^2(T_3,T_2) + \mathcal{F}_{\mathrm{p}}^3(T_3,T_2)\mathcal{X}_{\mathrm{p}} - 24T_2(\mathcal{X}_{\mathrm{p}})^2\right) \end{bmatrix} \qquad \mathcal{F}_{\mathrm{p}}^0(x,y) = 2(x^2+y^2) + 3xy$$

$$\mathcal{F}_{\mathrm{p}}^1(x,y) = 3\sqrt{2xy}\left(3(x+y) + \ell_{23}\right) \qquad \mathcal{F}_{\mathrm{p}}^2(x,y) = 6\ell_{23} - (4x+3y)$$

$$\mathcal{F}_{\mathrm{p}}^3(x,y) = \frac{6y}{\sqrt{2xy}}\left(\ell_{23} - (5x+y)\right) \qquad \mathcal{X}_{\mathrm{p}} = \cos\left(\frac{1}{3}\arccos\left(\frac{3\left(T_2+T_3-\ell_{23}\right)}{4\sqrt{2T_2T_3}}\right) + \frac{4\pi}{3}\right)$$

(19)

In the `Hexa` configuration, the parametrization is given by the following equation which is defined for $\chi \geq \frac{1}{6}$:

$$\mathcal{C}_{\mathrm{h}}^{\mathcal{V}}(\theta,\phi) = \frac{1}{96\ell_{23}} \begin{bmatrix} \frac{1}{T_2T_3}\mathcal{F}_{\mathrm{h}}^0(c_1,T_2,T_3) - 24(c_1-\ell_{23})\left(\sqrt{T_4}\mathcal{X}_{\mathrm{h}} + 2c_1\right) + \frac{12(\mathcal{X}_{\mathrm{h}})^2}{T_2T_3}\mathcal{F}_{\mathrm{h}}^1(c_1,T_2,T_3,T_4) \\ c_2\left(\frac{1}{(T_2)^2T_3}\mathcal{F}_{\mathrm{h}}^0(T_2,c_1,T_3) - 24(c_1-\ell_{23})\left(\frac{\sqrt{T_4}}{T_2}\mathcal{X}_{\mathrm{h}} + 2\right) + \frac{12(\mathcal{X}_{\mathrm{h}})^2}{(T_2)^2T_3}\mathcal{F}_{\mathrm{h}}^1(T_2,c_1,T_3,T_4)\right) \\ c_3\left(\frac{1}{T_2(T_3)^2}\mathcal{F}_{\mathrm{h}}^0(T_3,c_1,T_2) - 24(c_1-\ell_{23})\left(\frac{\sqrt{T_4}}{T_3}\mathcal{X}_{\mathrm{h}} + 2\right) + \frac{12(\mathcal{X}_{\mathrm{h}})^2}{T_2(T_3)^2}\mathcal{F}_{\mathrm{h}}^1(T_3,c_1,T_2,T_4)\right) \end{bmatrix}$$

(20)

$$\mathcal{F}_{\mathrm{h}}^0(x,y,z) = 3x^4 - (y-z)^4 - 8x^3(y+z) + 6x^2(8yz + (y-z)^2) \qquad T_4 = 4c_1T_3 - (c_1 - T_2 + T_3)^2$$

$$\mathcal{F}_{\mathrm{h}}^1(x,y,z,t) = (2(x^2 - (y-z)^2) - t)t \qquad \mathcal{X}_{\mathrm{h}} = \cos\left(\frac{1}{3}\arccos\left(\frac{6(c_1-\ell_{23})T_2T_3}{(T_4)^{\frac{3}{2}}}\right) + \frac{4\pi}{3}\right)$$

The partial derivatives can be easily computed by applying the chain rule to the aforementioned formulas. Since these are essentially polynomial functions or square roots, we do not provide them in this article and instead, we recall the following useful relations: $\partial_\theta T_2 = c_2\left(1 + \left(\frac{T_2}{c_2}\right)^2\right)$, $\partial_\theta T_3 = \frac{T_2T_3}{c_2}$, $\partial_\phi T_2 = 0$, and $\partial_\phi T_3 = -c_3\csc(\phi)^2\sec(\theta)$. To evaluate the non-trivial partial derivatives of $\mathcal{X}_{\mathrm{p}}$ and $\mathcal{X}_{\mathrm{h}}$ defined in (19) and (20), respectively, use the following formulas:

$$\partial_\alpha \mathcal{X}_{\mathrm{p}} = \frac{\frac{\partial_\alpha T_2}{T_2}\left(\ell_{23} + T_2 - T_3\right) + \frac{\partial_\alpha T_3}{T_3}\left(\ell_{23} - (T_2 - T_3)\right)}{8\sqrt{2T_2T_3}(4(\mathcal{X}_{\mathrm{p}})^2 - 1)}$$

$$\partial_\alpha \mathcal{X}_{\mathrm{h}} = \frac{(c_1 - \ell_{23})(2T_4(T_2\partial_\alpha T_3 + T_3\partial_\alpha T_2) - 3T_2T_3\partial_\alpha T_4)}{(4(\mathcal{X}_{\mathrm{h}})^2 - 1)(T_4)^{\frac{5}{2}}} \qquad \text{with } \alpha = \theta \text{ or } \phi \qquad (21)$$

### 3.3. Algorithm to evaluate the objective function and its partial derivatives

#### 3.3.1. Introduction

In the former section we presented the formulas to compute the centroid and its partial derivatives in the reference chart. In this section we will present the computation of the objective function and its gradient in the global chart that are required by the minimization algorithm. We denote $\mathcal{T}$ as the application that maps the coordinates from the global chart $(\theta,\phi)$ to the reference chart $(\tilde{\theta},\tilde{\phi})$ and is defined by:

$$(\tilde{\theta},\tilde{\phi}) = \mathcal{T}(\theta,\phi) \qquad (22)$$

From figure 4, it is clear that any point in the global chart can be transformed to the reference chart with the following operations. First, if the point lies in the northern hemisphere, it is transformed to the southern hemisphere by a reflection with respect to the plane $\{z = \frac{c_3}{2}\}$. The point is then mapped into the local chart with one or two quarter turns around the third axis. Finally, the point is mapped to the reference chart with

9

a rotation along the main diagonal of the hexahedron which can be seen as a composition of two quarter turns.

To keep track of these transformations during the algorithm we chose to use a permutation table associated with a set of signs. We denote $\sigma$ as the permutation table — or simply *permutation* — and $\mathsf{s}$ as the set of signs. In equation (23) the permutation and the set of signs are developed for a set of 3 elements.

$$\sigma = (\sigma_1 \ \sigma_2 \ \sigma_3) \qquad \mathsf{s} = \{\mathsf{s}_1, \mathsf{s}_2, \mathsf{s}_3\} \tag{23}$$

The permutation $(\sigma_1 \ \sigma_2 \ \sigma_3)$ means that the element in position $i$ goes to position $\sigma_i$ where each $\sigma_i$ is unique and $\sigma_i \in \{1, 2, 3\}$. Figure 7 shows an example of the permutations. The composition of two permutations $\tau$ and $\sigma$ is given by $\sigma \circ \tau = (\sigma_{\tau_1} \ \sigma_{\tau_2} \ \sigma_{\tau_3})$ or, with a permutation table, $\sigma \circ (i \ j \ k) = (\sigma_i \ \sigma_j \ \sigma_k)$. The inverse of a permutation, denoted $\sigma^{-1}$ is defined by the relation $\sigma^{-1} \circ \sigma = (1 \ 2 \ 3)$.

For the set of signs, each element verifies the relation $\mathsf{s}_i = \pm 1$. We define the composition of two sets of signs $\mathsf{s}$ and $\mathsf{s}'$ as $\mathsf{s}' \circ \mathsf{s} = \{\mathsf{s}'_1, \mathsf{s}'_2, \mathsf{s}'_3\} \circ \{\mathsf{s}_1, \mathsf{s}_2, \mathsf{s}_3\} = \{\mathsf{s}'_1 \mathsf{s}_1, \mathsf{s}'_2 \mathsf{s}_2, \mathsf{s}'_3 \mathsf{s}_3\}$ and is similar to the Hadamard product of two matrices. A permutation can be applied to a set of signs by the relation (24) which is denoted by a centered dot to distinguish it from the composition.

$$\sigma \cdot \{\mathsf{s}_1, \mathsf{s}_2, \mathsf{s}_3\} = \{\mathsf{s}_{\sigma_1^{-1}}, \mathsf{s}_{\sigma_2^{-1}}, \mathsf{s}_{\sigma_3^{-1}}\} \tag{24}$$

This definition holds for any set of three elements, for instance $\sigma \cdot \boldsymbol{n} = (n_{\sigma_1^{-1}}, n_{\sigma_2^{-1}}, n_{\sigma_3^{-1}})$.

To illustrate these notations, consider the following three examples. A reflection with respect to the plane $\{z = \frac{c_3}{2}\}$ is represented by the compositions $\sigma \leftarrow (1 \ 2 \ 3) \circ \sigma$ and $\mathsf{s} \leftarrow \{1, 1, -1\} \circ \mathsf{s}$. A quarter turn of $+\frac{\pi}{2}$ around the third axis is represented by $\sigma \leftarrow (2 \ 1 \ 3) \circ \sigma$ and $\mathsf{s} \leftarrow \{-1, 1, 1\} \circ \mathsf{s}$. Finally, a clockwise rotation around the main diagonal, as shown in figure 7, is represented by $\sigma \leftarrow (3 \ 1 \ 2) \circ \sigma$ and $\mathsf{s} \leftarrow (3 \ 1 \ 2) \cdot \mathsf{s}$.

From these definitions, the transformation $\mathcal{T}$ is found by solving the following equation for $\tilde{\theta}$ and $\tilde{\phi}$ where $\boldsymbol{n}$ is defined in equation (6).

$$\boldsymbol{n}(\tilde{\theta}, \tilde{\phi}) = \mathsf{s} \circ \left(\sigma \cdot \boldsymbol{n}(\theta, \phi)\right) \tag{25}$$

For example, when $\sigma = (3 \ 1 \ 2)$ and $\mathsf{s} = \{\mathsf{s}_1, \mathsf{s}_2, \mathsf{s}_3\}$, we get:

$$\mathcal{T}(\theta, \phi) = \begin{bmatrix} \operatorname{arccot}(\mathsf{s}_1 \mathsf{s}_2 \sin(\theta) \tan(\phi)) \\ \arccos(\mathsf{s}_3 \cos(\theta) \sin(\phi)) \end{bmatrix} \tag{26}$$

Since the transformation of the hexahedron preserves the distances, the objective function can be written in the reference chart:

$$\mathcal{F}(\theta, \phi) = |\mathcal{C}^{\mathcal{V}}(\theta, \phi) - \mathcal{C}^\star|^2 = |\mathcal{C}^{\mathcal{V}}(\mathcal{T}(\theta, \phi)) - \mathcal{C}^\star_{\text{ref}}|^2 = \mathcal{F}_{\text{ref}}(\mathcal{T}(\theta, \phi))$$

where $\mathcal{C}^\star_{\text{ref}}$ denotes the reference centroid transformed to the reference chart. It is obtained by applying the permutation to the coordinates of the reference centroid $\mathcal{C}^\star_{\text{ref}} \leftarrow \sigma \cdot \mathcal{C}^\star$ and then by applying the reflection $(\mathcal{C}^\star_{\text{ref}})_i \leftarrow c_i - (\mathcal{C}^\star_{\text{ref}})_i$ if $\mathsf{s}_i = -1$. As a result, the value of the objective function in the global chart is equal to the value of the objective function in the reference chart. The computation of the gradient in the global chart is a little more tricky and is given by:

$$\begin{bmatrix} \partial_\theta \mathcal{F}(\theta, \phi) \\ \partial_\phi \mathcal{F}(\theta, \phi) \end{bmatrix} = [\nabla_{(\theta, \phi)} \mathcal{T}(\theta, \phi)]^T \begin{bmatrix} \partial_{\tilde{\theta}} \mathcal{F}_{\text{ref}}(\tilde{\theta}, \tilde{\phi}) \\ \partial_{\tilde{\phi}} \mathcal{F}_{\text{ref}}(\tilde{\theta}, \tilde{\phi}) \end{bmatrix} \tag{27}$$

where $\nabla_{(\theta, \phi)} \mathcal{T}$ is the gradient of the transformation given by:

$$\nabla_{(\theta, \phi)} \mathcal{T} = \begin{bmatrix} \partial_\theta \mathcal{T}_\theta & \partial_\phi \mathcal{T}_\theta \\ \partial_\theta \mathcal{T}_\phi & \partial_\phi \mathcal{T}_\phi \end{bmatrix} \tag{28}$$

We propose a 3-stage algorithm to evaluate the objective function and its gradient. The first stage consists to find $\sigma$ and $\mathsf{s}$ to transform the given coordinates $(\theta, \phi)$ from the global chart to the reference chart $(\tilde{\theta}, \tilde{\phi})$. The second stage consists to evaluate the centroid, its partial derivatives, and the gradient of the objective function in the reference chart. The third, and final stage, consists to compute gradient of the objective function in the global chart with equation (27).

### 3.3.2. Stage 1: Transformation to reference chart

The first stage of the algorithm consists to transform the spherical coordinates $(\theta, \phi)$ to the reference chart. The output of this algorithm is the transformed coordinates $(\tilde{\theta}, \tilde{\phi})$, the permutation $\sigma$, and the set of signs $\mathsf{s}$. This transformation must be seen as a composition of reflections and rotations of the hexahedron. Imagine a point inside of a hexahedron on the locus of the centroid represented in figure 4. This point follows the transformation applied to the hexahedron. We would like to rotate the hexahedron in such a way that the point lies in the region close to the corner of the origin and close to the $\mathtt{QuadFace}$ of the plane $\{y = 0\}$. This region corresponds approximately to the location of the reference chart. To better understand this procedure, consider the example presented in figure 6. This figure represents the global chart for $\chi = 0.1$, $c_1 = 2$, $c_2 = 1.5$ and $c_3 = 1$. The spherical coordinates of the point $(\theta, \phi)$ denoted by 1 are located in the $[-\frac{\pi}{2}, 0] \times [\frac{\pi}{2}, \pi]$ region. The set of signs and the permutation are initialized to the identity $\mathsf{s} = \{1, 1, 1\}$ and $\sigma = (1\ 2\ 3)$. To construct the point 2, the coordinate $\phi$ of the point 1 is restricted to the interval $[0, \frac{\pi}{2}]$ with a reflection of the hexahedron on the $\{z = \frac{c_3}{2}\}$ plane. The set of signs becomes $\{1, 1, -1\}$. The point 3 is constructed by a rotation of $\frac{\pi}{2}$ around the third axis. This rotation corresponds to a permutation of the first axis and the second axis and by reversing the direction on the first axis. Thus, the permutation becomes $(2\ 1\ 3)$ and the sign becomes $\{-1, 1, -1\}$. Note that, at this point, figure 6 no longer represent the global map. The hexahedron has been rotated but the frame of spherical coordinates has not been changed. Thus, the representation in spherical coordinates should be redrawn by permuting the dimensions $c_1$ and $c_2$ of the hexahedron. Now, the point 3 is now located in the local chart defined in figure 5 but not on the reference chart. To place the point on the reference chart, the hexahedron must be rotated around its main diagonal like represented in figure 7. The direction of the rotation depends on the relative position of point 3 with respect to the limit curve $\phi_{\mathrm{rot}}^{\mathrm{lim}}$. Here, a counterclockwise rotation must be applied to the hexahedron which corresponds to a clockwise rotation on the global map. The permutation $(2\ 3\ 1)$ must be applied to the current permutation and to the set of signs resulting in the final permutation $\sigma = (3\ 2\ 1)$ and the set of signs $\mathsf{s} = \{-1, -1, 1\}$.
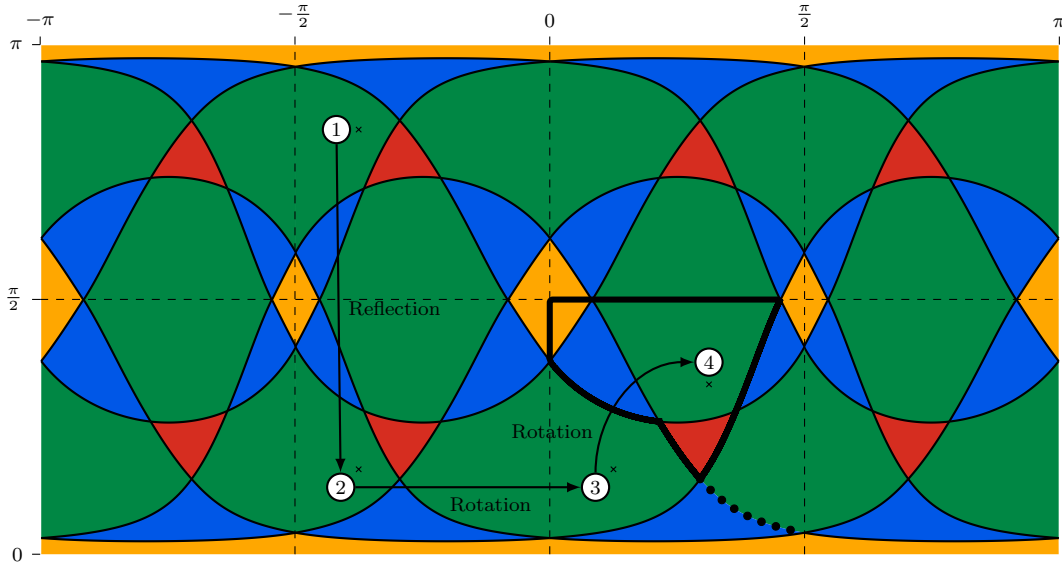


Figure 6: Illustration of the transformation of a point $(\theta, \phi)$ from the global chart to the reference chart. (1) The initial point. (2) The coordinate $\phi$ is restricted to $[0, \frac{\pi}{2}]$ with a reflection on the $\{z = \frac{c_3}{2}\}$ plane. (3) The coordinate $\theta$ is restricted to $[0, \frac{\pi}{2}]$ with a rotation around the third axis. (4) The point is rotated around the main diagonal of the hexahedron to fit in the reference chart.

We propose the following 7-step algorithm to transform the coordinates from the global chart to the reference chart. Each time the keyword **return** is encountered, the remaining instructions and steps must be ignored.

*Step 1.* Set $\tilde{\theta} \leftarrow \theta$ and $\tilde{\phi} \leftarrow \phi$.

*Step 2.* Translate $\tilde{\theta}$ and $\tilde{\phi}$ such that $(\tilde{\theta}, \tilde{\phi}) \in\ ]-\pi, \pi] \times [0, \pi]$ by adding $\pm\pi$ as many times as necessary.

*Step 3.* Initialize $\sigma \leftarrow (1\ 2\ 3)$ and $\mathsf{s} \leftarrow \{1, 1, 1\}$.

*Step 4.* Crop $\tilde{\theta}$ to $[0, \frac{\pi}{2}[$ and $\tilde{\phi}$ to $]0, \frac{\pi}{2}]$ with the following instructions:

- **If** $\tilde{\phi} \in [\frac{\pi}{2}, \pi]$, make a reflection on the third axis: $\tilde{\phi} \leftarrow \pi - \tilde{\phi}$ and $\mathsf{s} \leftarrow \{1, 1, -1\} \circ \mathsf{s}$.

- **If** $\tilde{\phi} = 0$, rotate by $\frac{\pi}{2}$ around the second axis: $\tilde{\theta} \leftarrow 0$, $\tilde{\phi} \leftarrow \frac{\pi}{2}$, $\sigma \leftarrow (2\ 1\ 3) \circ \sigma$, $\mathsf{s} \leftarrow \{-1, 1, 1\} \circ \mathsf{s}$, $\mathsf{s} \leftarrow \sigma \cdot \mathsf{s}$, and **return**.

- **If** $\tilde{\theta} = \pi$, rotate by $-\pi$ around the third axis: $\tilde{\theta} \leftarrow 0$ and $\mathsf{s} \leftarrow \{-1, -1, 1\} \circ \mathsf{s}$.

- **If** $\tilde{\theta} \in [\frac{\pi}{2}, \pi[$, rotate by $-\frac{\pi}{2}$ around the third axis: $\tilde{\theta} \leftarrow \tilde{\theta} - \frac{\pi}{2}$, $\sigma \leftarrow (2\ 1\ 3) \circ \sigma$, and $\mathsf{s} \leftarrow \{1, -1, 1\} \circ \mathsf{s}$.

- **If** $\tilde{\theta} \in\ ]-\pi, -\frac{\pi}{2}[$, rotate by $\pi$ around the third axis: $\tilde{\theta} \leftarrow \tilde{\theta} + \pi$ and $\mathsf{s} \leftarrow \{-1, -1, 1\} \circ \mathsf{s}$.

- **If** $\tilde{\theta} \in [-\frac{\pi}{2}, 0[$, rotate by $\frac{\pi}{2}$ around the third axis: $\tilde{\theta} \leftarrow \tilde{\theta} + \frac{\pi}{2}$, $\sigma \leftarrow (2\ 1\ 3) \circ \sigma$, and $\mathsf{s} \leftarrow \{-1, 1, 1\} \circ \mathsf{s}$.

*Step 5.* Apply the permutation to the dimensions of the hexahedron $\{c_1, c_2, c_3\} \leftarrow \sigma \cdot \{c_1, c_2, c_3\}$.

*Step 6.* Check whether the transformed angles belongs to the reference chart with the following instructions: check whether $(\tilde{\theta}, \tilde{\phi})$ belong to the reference chart using $\phi_{\mathrm{t1}}^{\mathrm{lim}}$, $\phi_{\mathrm{t2}}^{\mathrm{lim}}$ (12), $\phi_{\mathrm{p3}}^{\mathrm{lim}}$ (13c), and $\phi_{\mathrm{qe}}^{\mathrm{lim}}$ (14a) if $\chi < \frac{1}{6}$, otherwise, use $\phi_{\mathrm{p3}}^{\mathrm{lim}}$ (13c), $\phi_{\mathrm{qe}}^{\mathrm{lim}}$ (14a), $\phi_{\mathrm{h2}}^{\mathrm{lim}}$ (15b), and $\phi_{\mathrm{h3}}^{\mathrm{lim}}$ (15c). **If** the angles belong to the reference chart, then **return**.
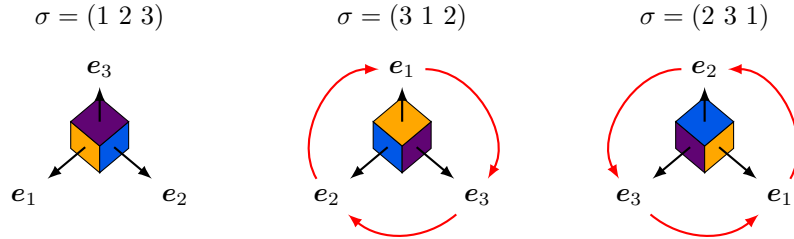


Figure 7: Illustration of the rotations to apply to the hexahedron to transform the angles to the reference chart. The left picture represents the identity. The picture in the middle represents a clockwise rotation. The right picture represents a counterclockwise rotation.

*Step 7.* Rotate the hexahedron around its main diagonal with the following instructions. We have to decide if we have to turn clockwise or counterclockwise. Figure 7 illustrates these rotations. The formulas given in this step to transform the coordinates from the local chart to the reference chart come from equation (25) using the appropriate set of signs and permutation like in (26).

- **If** $(\tilde{\theta}, \tilde{\phi})$ belongs to the region above $\phi_{\mathrm{rot}}^{\mathrm{lim}}$ (14b), rotate clockwise:
  $(\tilde{\theta}, \tilde{\phi}) \leftarrow \big(\mathrm{arccot}(\sin(\tilde{\theta})\tan(\tilde{\phi})), \arccos(\cos(\tilde{\theta})\sin(\tilde{\phi}))\big)$, $\sigma \leftarrow (3\ 1\ 2) \circ \sigma$, $\mathsf{s} \leftarrow (3\ 1\ 2) \cdot \mathsf{s}$ and **return**.

- **If** $(\tilde{\theta}, \tilde{\phi})$ belongs to the region below $\phi_{\mathrm{rot}}^{\mathrm{lim}}$ (14b), rotate counterclockwise:
  $(\tilde{\theta}, \tilde{\phi}) \leftarrow \big(\arctan(\cos(\tilde{\theta})\tan(\tilde{\phi})), \arccos(\sin(\tilde{\theta})\sin(\tilde{\phi}))\big)$, $\sigma \leftarrow (2\ 3\ 1) \circ \sigma$, $\mathsf{s} \leftarrow (2\ 3\ 1) \cdot \mathsf{s}$ and **return**.

At the end of this stage, we have determined $\sigma$, $\mathsf{s}$, and $(\tilde{\theta}, \tilde{\phi})$ which belong to the reference chart.

### 3.3.3. Stage 2: Compute the objective function and its gradient in the reference chart

The second stage of the algorithm consists to evaluate the centroid and its partial derivatives in the reference chart and to compute the gradient of the objective function. First, determine in which configuration — `Triangle`, `Penta`, `QuadEdge`, `QuadFace`, or `Hexa` — the transformed coordinates belong to using the internal limits $\phi_{\text{t3}}^{\text{lim}}$ (12), $\phi_{\text{p1}}^{\text{lim}}$ (13a), $\phi_{\text{p2}}^{\text{lim}}$ (13b) and $\phi_{\text{h1}}^{\text{lim}}$ (15a). If $\chi = \frac{1}{2}$, consider only the limit $\phi_{\text{p1}}^{\text{lim}}$ which is the same limit as $\phi_{\text{h1}}^{\text{lim}}$, but with a simpler expression. Note that $\theta_4^{\text{h}}$ can be placed before or after $\theta_5$ when $\chi > \frac{1}{6}$ depending on the dimensions of the hexahedron. However, they are always greater than $\theta_3$. Then, evaluate accordingly the centroid and the derivatives using the formulas defined in section 3.2.2. Finally, compute the gradient of the objective function using relation (8).

At the end of this stage, we have determined $\mathcal{F}_{\text{ref}}(\tilde{\theta}, \tilde{\phi})$, $\partial_{\tilde{\theta}} \mathcal{F}_{\text{ref}}(\tilde{\theta}, \tilde{\phi})$ and $\mathcal{F}_{\text{ref}}(\tilde{\theta}, \tilde{\phi})$.

### 3.3.4. Stage 3: Compute the gradient of the objective function in the global chart

The third and final stage consists to compute gradient of the objective function in the global chart using the formula (27). In the following, we give the expressions of the transpose of the gradient of the transformation for every $\sigma$. Note that the angles in these equations are the global angles $(\theta, \phi)$ and not the transformed angles $(\tilde{\theta}, \tilde{\phi})$. Furthermore, the minimization algorithm does not guarantee that the angles remain in $[-\pi, \pi] \times [0, \pi]$, so we ensure the validity of the below formulas with the modulo function.

- **If** $\sigma = (1\ 2\ 3)$:  **If** $\mathrm{mod}(\phi, 2\pi) \geq \pi$, $\mathsf{s}_3 \leftarrow -\mathsf{s}_3$,  $[\nabla_{(\theta,\phi)} \mathcal{T}]^T = \begin{bmatrix} \mathsf{s}_1 \mathsf{s}_2 & 0 \\ 0 & \mathsf{s}_3 \end{bmatrix}$

- **If** $\sigma = (1\ 3\ 2)$:  $[\nabla_{(\theta,\phi)} \mathcal{T}]^T = \begin{bmatrix} \mathsf{s}_1 \mathsf{s}_2 \frac{\sin(\theta)\sin(\phi)\cos(\phi)}{(\cos(\theta)\sin(\phi))^2 + \cos(\phi)^2} & -\mathsf{s}_3 \frac{\cos(\theta)\sin(\phi)}{\sqrt{1-(\sin(\theta)\sin(\phi))^2}} \\ -\mathsf{s}_1 \mathsf{s}_2 \frac{\cos(\theta)}{(\cos(\theta)\sin(\phi))^2 + \cos(\phi)^2} & -\mathsf{s}_3 \frac{\sin(\theta)\cos(\phi)}{\sqrt{1-(\sin(\theta)\sin(\phi))^2}} \end{bmatrix}$

- **If** $\sigma = (2\ 1\ 3)$:  **If** $\mathrm{mod}(\phi, 2\pi) \geq \pi$, $\mathsf{s}_3 \leftarrow -\mathsf{s}_3$,  $[\nabla_{(\theta,\phi)} \mathcal{T}]^T = \begin{bmatrix} -\mathsf{s}_1 \mathsf{s}_2 & 0 \\ 0 & \mathsf{s}_3 \end{bmatrix}$

- **If** $\sigma = (2\ 3\ 1)$:  $[\nabla_{(\theta,\phi)} \mathcal{T}]^T = \begin{bmatrix} -\mathsf{s}_1 \mathsf{s}_2 \frac{\cos(\theta)\sin(\phi)\cos(\phi)}{(\sin(\theta)\sin(\phi))^2 + \cos(\phi)^2} & \mathsf{s}_3 \frac{\sin(\theta)\sin(\phi)}{\sqrt{1-(\cos(\theta)\sin(\phi))^2}} \\ -\mathsf{s}_1 \mathsf{s}_2 \frac{\sin(\theta)}{(\sin(\theta)\sin(\phi))^2 + \cos(\phi)^2} & -\mathsf{s}_3 \frac{\cos(\theta)\cos(\phi)}{\sqrt{1-(\cos(\theta)\sin(\phi))^2}} \end{bmatrix}$

- **If** $\sigma = (3\ 1\ 2)$:  $[\nabla_{(\theta,\phi)} \mathcal{T}]^T = \begin{bmatrix} -\mathsf{s}_1 \mathsf{s}_2 \frac{\sin(\theta)\tan(\phi)}{1+(\cos(\theta)\tan(\phi))^2} & -\mathsf{s}_3 \frac{\cos(\theta)\sin(\phi)}{\sqrt{1-(\sin(\theta)\sin(\phi))^2}} \\ \mathsf{s}_1 \mathsf{s}_2 \frac{\cos(\theta)}{(\cos(\theta)\sin(\phi))^2 + \cos(\phi)^2} & -\mathsf{s}_3 \frac{\sin(\theta)\cos(\phi)}{\sqrt{1-(\sin(\theta)\sin(\phi))^2}} \end{bmatrix}$

- **If** $\sigma = (3\ 2\ 1)$:  $[\nabla_{(\theta,\phi)} \mathcal{T}]^T = \begin{bmatrix} \mathsf{s}_1 \mathsf{s}_2 \frac{\cos(\theta)\sin(\phi)\cos(\phi)}{(\sin(\theta)\sin(\phi))^2 + \cos(\phi)^2} & \mathsf{s}_3 \frac{\sin(\theta)\sin(\phi)}{\sqrt{1-(\cos(\theta)\sin(\phi))^2}} \\ \mathsf{s}_1 \mathsf{s}_2 \frac{\sin(\theta)}{(\sin(\theta)\sin(\phi))^2 + \cos(\phi)^2} & -\mathsf{s}_3 \frac{\cos(\theta)\cos(\phi)}{\sqrt{1-(\cos(\theta)\sin(\phi))^2}} \end{bmatrix}$

Although it is not required by the algorithm, the centroid given in the reference chart can be transformed to the global chart by applying the inverse of the permutation to its coordinates $\mathcal{C} \leftarrow \sigma^{-1} \cdot \mathcal{C}_{\text{ref}}$ and to the set of signs $\mathsf{s} \leftarrow \sigma^{-1} \circ \mathsf{s}$, and then by applying the correction $\mathcal{C}_i \leftarrow c_i - \mathcal{C}_i$ if $\mathsf{s}_i = -1$.

## 4. Numerical results

### 4.1. Introduction

In this section, we demonstrate that the proposed analytic method outperforms the geometric approaches. Two criteria are evaluated: the runtime and the robustness. The former criterion is essential to reduce the wall clock time and total CPU time, especially for high performance computers while the latter is necessary to evaluate the consistency of the accuracy of the results.

Three geometric approaches are compared to our proposed method. The first, referred to as *finite differences gradient*, consists to reconstruct an approximation $\omega \in \mathfrak{A}$ (2) in the direction $\boldsymbol{n}$ using the flood

algorithm proposed by Diot & François [24]. The centroid of this approximation is computed using a formula for convex polyhedrons as presented in [25]. The partial derivatives of the centroid are evaluated with a centered finite-difference scheme which requires two more reconstructions per direction. The gradient of the objective function is then computed using formula (8). Overall, five calls to the flood algorithm are required to compute the centroid and the gradient of the objective function. The second method, referred to as *geometric gradient*, consists to use only one call of the flood algorithm to compute the centroid and to evaluate the gradient by the method of Chen & Zhang [17], which we have summarized using our notations in Appendix A. This second method requires to construct the vertex–face connectivities of the polyhedron at the term of the flood algorithm to finally compute its centroid. In Appendix B, we propose a set of formulas to compute the centroid directly during the flood algorithm. The third method, referred to as *optimized centroid*, is an improvement of the second method where we use these formulas to compute the centroid.

In [24], the polyhedron is rotated such that the flood direction $\boldsymbol{n}$ corresponds to the axis $\boldsymbol{e}_3$. Two special cases must be treated if $\boldsymbol{n} = \pm\boldsymbol{e}_3$. When the partial derivatives are evaluated by finite differences near the poles, the singularity of the rotation creates some non-negligible perturbations in the values of the partial derivatives. Since the minimization algorithm relies on the accuracy of the derivatives, it is necessary to avoid the rotation. In Appendix B, we describe how to adapt the algorithm for any flood direction. This improvement is used in any geometric method tested in this paper.

All of these methods are implemented in the massively parallel open-source code Notus [26] which is dedicated to the modelization and simulation of incompressible fluid flows. Its numerical framework is the finite volume method on Cartesian staggered grids with a methodological focus on interfaces treatment (multi-material interface advection [18], surface tension computation [27], immersed boundary methods [28], *etc.*). The verification cases are conducted on a supercomputer with Intel Xeon E5-4640 processors and on a supercomputer with Intel Xeon E5-2690V3 processors. The code was compiled with Intel Fortran Compiler 18.0. Althought the runtime ratios given in this article are implementation-dependent and may vary with the architecture and the compilers, they are representative of the general behaviour of the methods.

### 4.2. Runtime ratios

To determine the performances of the various methods, the evaluation of the objective function and its gradient are computed for a large number of configurations. The ratio between the runtime of the methods and the runtime of our proposed method is then calculated. To generate the different cases, the direction $\boldsymbol{n}$ and the volume fraction $\chi$ are evenly sampled. We found that the dimensions of the cell do not change the runtime ratios.

We use a linear sampling for the volume fraction $\chi$ in the range $10^{-4}$ to $\frac{1}{2}$. To sample the direction $\boldsymbol{n}$, we cannot use a linear sampling on $\theta$ and $\phi$ as it does not evenly distribute the points on the unit sphere since the poles are more densely sampled than the equator. Instead, the points on the sphere are generated along a spherical Fibonacci grid [29] which gives a good approximation of an evenly distribution of points on the sphere. The coordinates of these points are given in equation (29) for $2N + 1$ samples.

$$\forall k \in [\![-N, N]\!] \qquad \theta_k = 2\pi \frac{\mathrm{mod}(k, \varphi)}{\varphi} \qquad \phi_k = \arccos\left(\frac{2k}{2N+1}\right) \qquad \text{where } \varphi = \frac{1 + \sqrt{5}}{2} \qquad (29)$$

The results are presented in table 1 for 100 samples of $\chi$ and 250001 samples of $\boldsymbol{n}$. Increasing the number of samples does not significantly change the runtime ratios.

| Method | Runtime ratio |
|---|---|
| Finite differences gradient | 113.5 |
| Geometric gradient (Appendix A) | 28.7 |
| Optimized centroid (Appendix B) | 20.8 |
| **Analytic reconstruction** | **1.0** |

Table 1: Runtime ratio between geometric methods and analytic method.

From table 1, we observe that the geometric gradient method is almost 4 times faster than the finite differences gradient method. This result is expected since it replaces four calls to the flood algorithm with simple calculation on a polygon. The optimized centroid method that is proposed in Appendix B is 1.4 times faster than the geometric gradient method. This gain is obtained by computing the centroid directly during the flood algorithm instead of reconstructing a polyhedron structure to subsequently compute its centroid. Also using the method of Chen & Zhang [17] to compute the gradient makes the optimized centroid method 5.5 faster than the finite differences gradient method. Drastic increases in performance is further obtained through our proposed analytic method which is 113.5 times faster than the finite differences method and 20.8 times faster than the most competitive geometric method. These results show that the proposed method should be used to improve the numerical simulation runtime. The remainder of this section is devoted to demonstrate the robustness of our method.

### 4.3. Robustness

To verify the proposed method, the centroid and the gradient computed by the formulas given in section 3 have been compared to those given by the finite differences gradient method and the geometric gradient method for a large number of configurations. The parameters varied are the cell dimensions $\{c_1, c_2, c_3\}$, the direction $\boldsymbol{n}$, and the volume fraction $\chi$. Although the position of the reference centroid $\mathcal{C}^\star$ does not matter, it is wise to select a position far away from the locus of the centroids $\mathfrak{L}^\mathcal{V}$ to avoid to nullify the term $\mathcal{C}^\mathcal{V}(\theta, \phi) - \mathcal{C}^\star$ in the gradient of the objective function which may hide potential errors in the partial derivatives of the centroid. The center of the hexahedron is a good choice for the reference centroid.

Regardless of the parameters, the distance between two centroids given by the two different methods is close to the machine precision. However, the gradient of the objective function does differ between the methods. As expected, the difference between the gradients is given by finite differences and the proposed method is the highest. We found that the optimal value for the finite differences step is $\Delta\theta = \Delta\phi = 10^{-9}$ that results in a difference of about $10^{-8}$ in magnitude. With the method of Chen & Zhang [17], described in Appendix A, and the optimized centroid method discussed in Appendix B, this difference drops to the machine precision.

Although this verifies our method, we also tested the behavior of the various methods coupled with a minimization algorithm to further analyze their behavior. In this article, we chose the BFGS algorithm along with the line-search algorithm described in [30]. We use the classic initial guess based on the centroid of the cell $\mathcal{C}(\Omega)$ and the reference centroid $\mathcal{C}^\star$ defined in the following equation:

$$\boldsymbol{n}(\theta_0, \phi_0) = \frac{\mathcal{C}^\star - \mathcal{C}(\Omega)}{|\mathcal{C}^\star - \mathcal{C}(\Omega)|} \tag{30}$$

The objective function (7) contains several local minima and sometimes several global minima, such as the case where the reference centroid is at the center of the cell. We will exploit this property to measure the robustness of our proposed method compared to the others since the less robust methods are more likely to make the minimization algorithm fall into local minima.

For the line-search algorithm proposed in [30] we use the currently optimized parameters: $\rho = 0.25$, $\sigma = 0.5$, $\tau_1 = 3$, $\tau_2 = 0.1$ and $\tau_3 = 0.5$. The minimization algorithm is the same for all the tested methods and stops when it reaches a maximum number of iterations or the norm of the gradient of the objective function falls below a prescribed tolerance value.

We have conducted the robustness study on two sets of one million random-generated cases. In both sets, the dimensions of the cell for each case are computed with the formula $c_i = \alpha_i \cdot 10^\beta$ where $\alpha_i \in [0.1, 1[$ and $\beta \in [-3, 3]$ are randomly-generated with a uniform distribution. The volume fractions $\chi \in [10^{-3}, \frac{1}{2}]$ are generated the same way. The two sets differ by the way the reference centroids are generated. In the first set, the reference centroids lie on the locus of the centroids. That means that the minimum value of the objective function (7) is zero. This set will be referred to as the *exact* reconstruction cases. To generate this set, a direction $\boldsymbol{n}$ is randomly generated with a uniform distribution and a flood algorithm is used to compute the reference centroids. In the second set, the reference centroids are randomly generated over the cell with a uniform distribution. This set will be referred to as the *random* reconstruction cases. The

tolerance value of the BFGS algorithm — the norm of the gradient of the objective function — is set to $10^{-14}$ and the maximum number of iterations is set to 400. These parameters can be relaxed for a practical use of MOF, but here, we want to detect whether one of the methods prevents to reach a small residual.

### 4.3.1. Robustness on exact reconstructions with a BFGS algorithm

On the exact reconstruction cases, the four methods — finite differences gradient, geometric gradient, optimized centroid, and analytical reconstruction — give the same statistical results. Note that each iteration of the BFGS algorithm requires one evaluation of the gradient and several iterations of the line-search algorithm. Each iteration of the line-search algorithm requires one evaluation of the gradient and at least one more for the bracketing phase. The median of the number of gradient evaluations in the BFGS is 10, the median of the number of gradient evaluations in the line-search algorithm is 47 and the median of the sum of gradient evaluations in the BFGS and line-search is 57.

We have evaluated the quality of the computed minimum for each pair of methods by comparing the final values of the objective function. With this criterion, we are not able to differentiate the methods since they give the same results with no apparent differences. We explain this behavior by remarking that the term $\mathcal{C}^{\mathcal{V}}(\theta, \phi) - \mathcal{C}^{\star}$ in the gradient vanishes when the BFGS gets closer to the minimum and, as a result, the numerical errors on the partial derivatives are reduced by this term. Furthermore, the initial guess makes this term quite small from the initial step of the algorithm. For the random reconstruction cases, this term does not vanish and we are able to see the differences.

### 4.3.2. Robustness of the random reconstructions with a BFGS algorithm

On the random reconstruction cases, the behavior of the BFGS with the finite differences gradient method differs from the other methods. Table 2 presents the median of the number of gradient evaluations in the BFGS, the line-search, and the sum of the BFGS and the line-search algorithms.

| Method | BFGS | line-search | BFGS + line-search |
|---|---|---|---|
| Finite differences gradient | 12 | 69 | 81 |
| Others | 11 | 53 | 64 |

Table 2: Median of the number of calls of the gradient in the different parts of the minimization algorithm and for the different reconstruction methods.

We remark that the finite differences gradient method requires more calls to the gradient than the other methods to find the minimum. This time, the term $\mathcal{C}^{\mathcal{V}}(\theta, \phi) - \mathcal{C}^{\star}$ does not vanish in the gradient of the objective function and the errors in the approximation of the partial derivatives deteriorates the convergence of the BFGS algorithm. When the final value of the objective function for the finite differences gradient method is compared to the value given by the other methods, in 83% of the cases, the other methods give a better result. On the contrary, when this value is compared between a pair of the other methods, the better results are equally distributed between both methods and close to each other.

To conclude, we have shown that the geometric gradient method, the optimized centroid method, and the analytic reconstruction methods offer the same accuracy. This is due to the absence of approximations in the evaluation of the partial derivatives of the objective function. These methods can be differentiated by their runtime and, as shown in table 1, our analytic reconstruction method is at least 20 times faster than the other methods.

## 5. Conclusion

In this article we have developed a new fast and robust approach to solve the minimization problem of the moment-of-fluid method in 3D on rectangular hexahedrons. The key idea is to find a global parametrization in spherical coordinates of the locus of the centroids at fixed volume. This allows to compute the objective function and its gradient with fully analytical formulas which avoid the use of a computationally intensive

geometric flood algorithm. The numerical results show that our analytical method is up to 100 times faster than the geometric approaches. We have also adapted and improved the flood algorithm [24] for the moment-of-fluid method for general convex cells. In future work, we will extend our methodology of the centroid locus parametrization to other cell shapes, for instance, in 2D on convex polygons or in 3D on tetrahedrons.

## Appendix A. Analytic gradient from the geometric approach

In this section, we present the formulas to compute the gradient of the objective function proposed by Chen & Zhang [17]. The input data of this algorithm is the surface of the intersection of a half-space with the polyhedron given by the flood algorithm. This surface will be denoted by $\mathfrak{P}$ and will be referred to as *top polygon*. Figure A.8 gives an example of a top polygon in the `Penta` configuration. The top polygon is composed of $n$ vertices denoted by $\boldsymbol{p}_i$ for $i \in [\![1, n]\!]$. The algorithm to compute the gradient of the objective function can be decomposed in four steps.
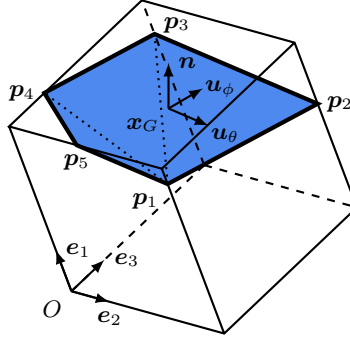


Figure A.8: Example of a top polygon (`Penta` configuration, $\chi = 0.9$). The points $\boldsymbol{p}_i$ denote the vertices of the polygon and $\boldsymbol{x}_G$ denotes the centroid of the top polygon. The Cartesian frame and the spherical frame are represented in there respective positions.

*Step 1.* Compute the surface $S$ and the centroid $\boldsymbol{x}_G$ of the top polygon $\mathfrak{P}$ in the Cartesian frame $(O; \boldsymbol{e}_1, \boldsymbol{e}_2, \boldsymbol{e}_3)$ with equations (A.1) and (A.2).

$$S = \frac{1}{2} \sum_{i=2}^{n-1} \left| (\boldsymbol{p}_i - \boldsymbol{p}_1) \times (\boldsymbol{p}_{i+1} - \boldsymbol{p}_1) \right| \tag{A.1}$$

$$\boldsymbol{x}_G = \boldsymbol{p}_1 + \frac{1}{6S} \sum_{i=2}^{n-1} \left| (\boldsymbol{p}_i - \boldsymbol{p}_1) \times (\boldsymbol{p}_{i+1} - \boldsymbol{p}_1) \right| \left( (\boldsymbol{p}_i - \boldsymbol{p}_1) + (\boldsymbol{p}_{i+1} - \boldsymbol{p}_1) \right) \tag{A.2}$$

*Step 2.* Transform the points into the spherical frame $(\boldsymbol{x}_G; \boldsymbol{u}_\theta, \boldsymbol{u}_\phi, \boldsymbol{n})$ where the origin is set to the centroid of the top polygon. The unit vectors of the spherical basis can be expressed in the Cartesian basis with equation (A.3).

$$\begin{aligned}
\boldsymbol{u}_\theta &= -\sin(\theta)\boldsymbol{e}_1 + \cos(\theta)\boldsymbol{e}_2 \\
\boldsymbol{u}_\phi &= \cos(\theta)\cos(\phi)\boldsymbol{e}_1 + \sin(\theta)\cos(\phi)\boldsymbol{e}_2 - \sin(\phi)\boldsymbol{e}_3 \\
\boldsymbol{n} &= \cos(\theta)\sin(\phi)\boldsymbol{e}_1 + \sin(\theta)\sin(\phi)\boldsymbol{e}_2 + \cos(\phi)\boldsymbol{e}_3
\end{aligned} \tag{A.3}$$

Any point $\boldsymbol{p}$ in the Cartesian frame can be transformed into a point $\tilde{\boldsymbol{p}}$ in the spherical frame by the relation (A.4).

$$\tilde{\boldsymbol{p}} = \begin{bmatrix} (\boldsymbol{p} - \boldsymbol{x}_G) \cdot \boldsymbol{u}_\theta \\ (\boldsymbol{p} - \boldsymbol{x}_G) \cdot \boldsymbol{u}_\phi \\ (\boldsymbol{p} - \boldsymbol{x}_G) \cdot \boldsymbol{n} \end{bmatrix} \tag{A.4}$$

17

*Step 3.* Calculate three quadratic integrals over the top polygon. Consider any polynomial function $\varphi\colon \mathbb{R}^3 \to \mathbb{R}$ of degree at most two. The integral of $\varphi$ over the top polygon can be exactly computed using the sum of a 3-point Gauss quadrature, as defined in formula (A.5). This formula comes from the decomposition of the polygon into triangles as represented by dotted lines in figure A.8. Note that the points must be transformed into the spherical frame using the previous relation (A.4).

$$I_\varphi = \frac{1}{6} \sum_{i=2}^{n-1} \left| (\tilde{\boldsymbol{p}}_i - \tilde{\boldsymbol{p}}_1) \times (\tilde{\boldsymbol{p}}_{i+1} - \tilde{\boldsymbol{p}}_1) \right| \left( \varphi\left( \frac{\tilde{\boldsymbol{p}}_i + \tilde{\boldsymbol{p}}_1}{2} \right) + \varphi\left( \frac{\tilde{\boldsymbol{p}}_i + \tilde{\boldsymbol{p}}_{i+1}}{2} \right) + \varphi\left( \frac{\tilde{\boldsymbol{p}}_{i+1} + \tilde{\boldsymbol{p}}_1}{2} \right) \right) \tag{A.5}$$

Compute the quantities $I_{xx}$, $I_{xy}$ and $I_{yy}$ which correspond, respectively, to $\varphi = x^2$, $\varphi = xy$ and $\varphi = y^2$. In these formulas, $x$, $y$ and $z$ are the coordinates of any point in the spherical frame given by $x\boldsymbol{u}_\theta + y\boldsymbol{u}_\phi + z\boldsymbol{n}$.

*Step 4.* Finally, compute the partial derivatives in the spherical frame and the gradient of the objective function. The partial derivatives in the spherical frame are computed using relation (A.6).

$$\begin{aligned}
\partial_\theta \widetilde{\mathcal{C}^\mathcal{V}}(\theta, \phi) &= \frac{\sin(\phi)}{\mathcal{V}} \left[ I_{xx}, I_{xy}, 0 \right] \\
\partial_\phi \widetilde{\mathcal{C}^\mathcal{V}}(\theta, \phi) &= -\frac{1}{\mathcal{V}} \left[ I_{xy}, I_{yy}, 0 \right]
\end{aligned} \tag{A.6}$$

The gradient of the objective function is computed with formula (A.7). Note that the centroid and the reference centroid must be transformed into the spherical frame using relation (A.4).

$$\begin{aligned}
\partial_\theta \mathcal{F}(\theta, \phi) &= 2 \left( \widetilde{\mathcal{C}^\mathcal{V}}(\theta, \phi) - \widetilde{\mathcal{C}}^\star \right) \cdot \partial_\theta \widetilde{\mathcal{C}^\mathcal{V}}(\theta, \phi) \\
\partial_\phi \mathcal{F}(\theta, \phi) &= 2 \left( \widetilde{\mathcal{C}^\mathcal{V}}(\theta, \phi) - \widetilde{\mathcal{C}}^\star \right) \cdot \partial_\phi \widetilde{\mathcal{C}^\mathcal{V}}(\theta, \phi)
\end{aligned} \tag{A.7}$$

## Appendix B. Improvements of the flood algorithm for the moment-of-fluid method

In this section, we present some optimizations related to the flood algorithm proposed by Diot & François [24]. The first optimization consists in getting rid of the rotation of the polyhedron in the reference frame since it induces some singularities in the derivative when $\boldsymbol{n} = \pm \boldsymbol{e}_3$. The second optimization consists in evaluating the centroid during the reconstruction.
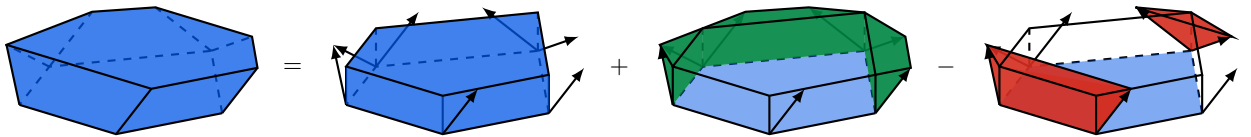


Figure B.9: Decomposition of a prismatoid in the sum of three terms. First, add a right prism. Second, add some tetrahedron and triangular prisms (in green). Third, subtract some tetrahedron and triangular prisms (in red). The arrows denote the unit tangent of the edges of the prismatoid.

The method proposed by Diot & François consists in bracketing the position of the interface between two parallel slices of the polyhedron. Each slice corresponds to a plane that passes through, at least, one vertex of the polyhedron. The slices are sorted in such a way that the distances of the planes on the flood axis $\boldsymbol{n}$ are in increasing order. The shape between two consecutive planes is a polyhedron called a *prismatoid*. All the vertices of a prismatoid are contained in one or the other plane as show by the example in figure B.9. The flood algorithm consists in computing the volume of the prismatoids one after the other until the reference volume is exceeded. Once the reference volume exceeded, the position of the interface is found inside the last prismatoid (refer to [24] for the method). Here, we propose an alternative method to compute the volume of the prismatoids for any direction $\boldsymbol{n}$ instead of $\boldsymbol{n} = \boldsymbol{e}_3$ in the original article. Then we present new formulas to evaluate their centroids.

In the article of Diot & François, the volume of a prismatoid is computed as the volume of a right prism plus the volume of some tetrahedrons and triangular prisms minus the volume of some tetrahedrons and triangular prisms (refer to figure B.9). In figure B.10, we present the notations of the known quantities during the computation of the volume. The base of the right prism is composed of $n$ vertices $(\boldsymbol{p}_i)_{i \in [\![1,n]\!]}$ that forms the bottom plane of the prismatoid and its height is denoted by $h$. The tetrahedron is generated by three unit vectors $\boldsymbol{u}$, $\boldsymbol{v}$ and $\boldsymbol{n}$. The triangular prism is generated by the flood direction $\boldsymbol{n}$ and the normal of one of its face $\boldsymbol{n}_f$.
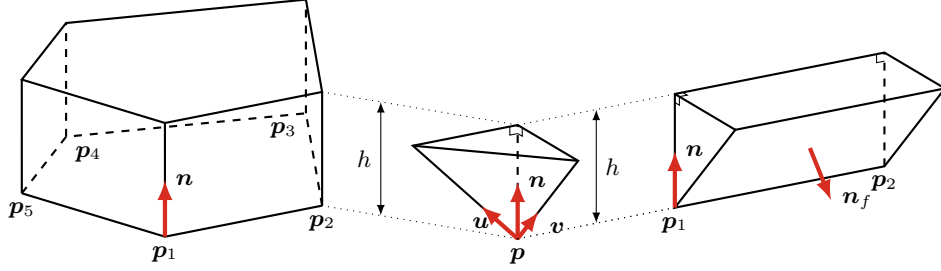


Figure B.10: Decomposition of the prismatoid. Left: right prism. Middle: tetrahedron. Left: triangular prism.

The volume of a tetrahedron and its centroid can be computed using equation (B.1).

$$\mathcal{V}_{\text{tetra}} = \frac{h^3}{6} \left( \frac{\boldsymbol{u}}{\boldsymbol{u} \cdot \boldsymbol{n}} \times \frac{\boldsymbol{v}}{\boldsymbol{v} \cdot \boldsymbol{n}} \right) \cdot \boldsymbol{n} \qquad \mathcal{C}_{\text{tetra}} = \boldsymbol{p} + \frac{h}{4} \left( \boldsymbol{n} + \frac{\boldsymbol{u}}{\boldsymbol{u} \cdot \boldsymbol{n}} + \frac{\boldsymbol{v}}{\boldsymbol{v} \cdot \boldsymbol{n}} \right) \tag{B.1}$$

The volume of a triangular prism and its centroid can be computed using equation (B.2).

$$\mathcal{V}_{\text{tri}} = -\frac{h^2}{2} \left( |\boldsymbol{p}_2 - \boldsymbol{p}_1| \frac{\boldsymbol{n} \cdot \boldsymbol{n}_f}{|\boldsymbol{n} \times \boldsymbol{n}_f|} \right) \qquad \mathcal{C}_{\text{tri}} = \frac{\boldsymbol{p}_1 + \boldsymbol{p}_2}{2} + \frac{h}{3} \left( \frac{\boldsymbol{n}_f \times (\boldsymbol{p}_2 - \boldsymbol{p}_1)}{|\boldsymbol{n} \times \boldsymbol{n}_f||\boldsymbol{p}_2 - \boldsymbol{p}_1|} \right) \tag{B.2}$$

The volume of a right prism and its centroid can be computed using equations (B.3a) and (B.3b).

$$S = \frac{1}{2} \sum_{i=2}^{n-1} |(\boldsymbol{p}_i - \boldsymbol{p}_1) \times (\boldsymbol{p}_{i+1} - \boldsymbol{p}_1)| \tag{B.3a}$$

$$\mathcal{V}_{\text{prism}} = hS \qquad \mathcal{C}_{\text{prism}} = \frac{h}{2}\boldsymbol{n} + \boldsymbol{p}_1 + \frac{1}{6S} \sum_{i=2}^{n-1} |(\boldsymbol{p}_i - \boldsymbol{p}_1) \times (\boldsymbol{p}_{i+1} - \boldsymbol{p}_1)| \left( (\boldsymbol{p}_i - \boldsymbol{p}_1) + (\boldsymbol{p}_{i+1} - \boldsymbol{p}_1) \right) \tag{B.3b}$$

The centroid of a prismatoid and the centroid of the final polyhedron are computed using the additivity of the first momentum, that is, using the pseudo-formula (B.4).

$$\mathcal{C} = \frac{\sum \mathcal{V}_{\text{tetra}} \mathcal{C}_{\text{tetra}} + \sum \mathcal{V}_{\text{tri}} \mathcal{C}_{\text{tri}} + \sum \mathcal{V}_{\text{prism}} \mathcal{C}_{\text{prism}}}{\sum \mathcal{V}_{\text{tetra}} + \sum \mathcal{V}_{\text{tri}} + \sum \mathcal{V}_{\text{prism}}} \tag{B.4}$$

Remark that it is more efficient to write the algorithm in terms of first momentum instead of centroid. The centroid of the final polyhedron can be easily computed by dividing its first momentum by the total volume which is equal to the reference volume.

## Appendix C. Proof of the formulas for the parametrization of the locus of the centroids

In this appendix, we give a proof of the formulas given in section 3. For each configuration — `Triangle`, `QuadEdge`, `QuadFace`, `Penta`, and `Hexa` — the same methodology is used to obtain the analytic formulas. First, we remark that the surface of the half-space intersects between three and six edges of the hexahedron. In each configuration, we denote $A$, $B$, and $C$ three of these intersection points. The other points, when they exist, can be deduced from the coordinates of these points since they belong to the same plane. We define $\alpha$, $\beta$, and $\gamma$ the coordinates of the points $A$, $B$, and $C$ on the respective directions of their edges. The volume and the centroid of the intersection of the half-space and the rectangular hexahedron is then computed by a tetrahedral decomposition and by using the additivity of the volume and the first momentum. We recall that the centroid of a tetrahedron is equal to the centroid of its vertices. Then, some inequalities between $\alpha$, $\beta$, and $\gamma$ are established from the geometric constraints of the different configurations. Next, the volume $\mathcal{V}$ is imposed to give a relation $\beta = \beta(\alpha, \gamma, \mathcal{V})$. At this step, the centroid is described locally as a function of $\alpha$ and $\gamma$ for a fixed volume $\mathcal{V}$. The definition domain $\mathcal{D}_\star^{\mathcal{V}}$ of the local parametrization and its limit curves in $(\alpha, \gamma)$ are given for each configuration. The concatenation of these domains is illustrated in figure C.11 for $\chi \leq \frac{1}{6}$ and $\chi > \frac{1}{6}$. The bold lines correspond to the reference chart in $(\alpha, \gamma)$ that map to the reference chart in $(\theta, \phi)$ shown in figure 5. Finally, we give the parametrizations and the associated limit curves in spherical coordinates $(\theta, \phi)$ defined in section 3.
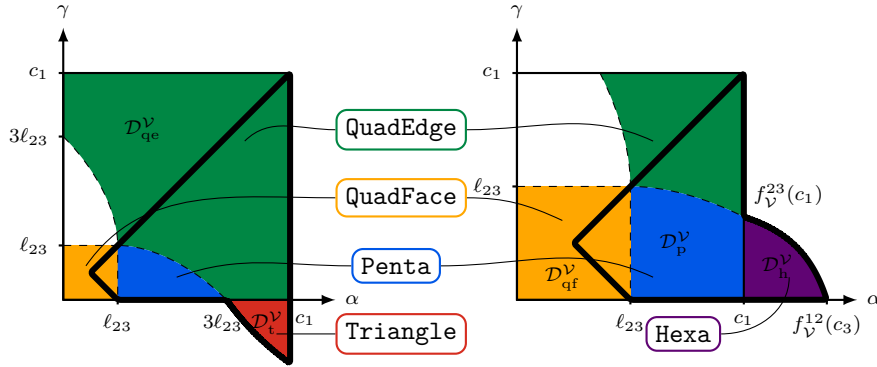


Figure C.11: Local charts in $(\alpha, \gamma)$ of all the configurations. The bold region corresponds to the reference chart. (left) $\chi \leq \frac{1}{6}$. (right) $\chi > \frac{1}{6}$.

### Appendix C.1. Definitions and notations

In the same way as for equation (6), the normal to the plane is defined as:

$$\boldsymbol{n} = \frac{1}{\sqrt{a_1^2 + a_2^2 + a_3^2}} \begin{bmatrix} a_1 \\ a_2 \\ a_3 \end{bmatrix} = \begin{bmatrix} \sin(\phi)\cos(\theta) \\ \sin(\phi)\sin(\theta) \\ \cos(\phi) \end{bmatrix} \tag{C.1}$$

where $\theta \in [-\pi, \pi]$ and $\phi \in [0, \pi]$ are the spherical coordinates. The interface $\mathfrak{P}$ defined in (10) can be alternatively defined by:

$$\mathfrak{P} = \left\{ (x, y, z) \in \mathbb{R}^3 \mid a_1 x + a_2 y + a_3 z = 1 \right\} \tag{C.2}$$

The coefficients $a_1$, $a_2$, and $a_3$ will be referred to as *coefficients of the plane*. We restrict $\theta$ to $[0, \pi/2]$ and $\phi$ to $[0, \pi/2]$ by symmetry, hence, $\cos(\phi)$, $\cos(\theta)$, $\tan(\phi)$, $\tan(\theta)$, $a_1$, $a_2$, and $a_3$ are positive. From (C.1), we have the relations:

$$\tan(\theta) = \frac{a_2}{a_1} \qquad \cot(\phi) = \frac{a_3}{a_1}\cos(\theta) \tag{C.3}$$

We consider a rectangular hexahedron $\Omega = [0, c_1] \times [0, c_2] \times [0, c_3]$. We recall that the reference volume is denoted by $\mathcal{V}$ and the associated volume fraction $\frac{\mathcal{V}}{c_1 c_2 c_3}$ is denoted by $\chi$. We make the assumption that

$\chi \le \frac{1}{2}$ since the case $\chi > \frac{1}{2}$ can be treated by considering the complementary problem. In this appendix, we use the following notations ($i, j \in \{1, 2, 3\}$) already defined in (11):

$$\ell_{ij} = \frac{2\mathcal{V}}{c_i c_j} \qquad T_1 = c_1 \cot(\theta) \qquad T_2 = c_2 \tan(\theta) \qquad T_3 = c_3 \cot(\phi) \sec(\theta)$$

The following functions will be used in the definition of the limit curves of the local charts. The roots of the following second degree polynomial in $\gamma$ given by $\gamma^2 + \alpha\gamma + \alpha^2 - 3\ell_{ij}\alpha = (\gamma - f_{\mathcal{V}}^{ij}(\alpha))(\gamma - \tilde{f}_{\mathcal{V}}^{ij}(\alpha))$ are equal to:

$$f_{\mathcal{V}}^{ij}(x) = \frac{1}{2}\left(-x + \sqrt{12\ell_{ij}x - 3x^2}\right) \qquad \tilde{f}_{\mathcal{V}}^{ij}(x) = \frac{1}{2}\left(-x - \sqrt{12\ell_{ij}x - 3x^2}\right) \tag{C.4}$$

The function $f_{\mathcal{V}}^{ij}$ is well defined and positive on $[0, 3\ell_{ij}]$, monotonically increasing on $[0, \ell_{ij}]$ and monotonically decreasing on $[\ell_{ij}, 3\ell_{ij}]$. It verifies the identities $f_{\mathcal{V}}^{ij}(0) = 0$, $f_{\mathcal{V}}^{ij}(\ell_{ij}) = \ell_{ij}$, and $f_{\mathcal{V}}^{ij}(3\ell_{ij}) = 0$. We also introduce $g_{\mathcal{V}}$ as:

$$g_{\mathcal{V}}(\alpha) = c_1 \frac{2\alpha^2 + (2c_3 - 3\ell_{12})\alpha - c_3^2 + \sqrt{(2\alpha^2 + (2c_3 - 3\ell_{12})\alpha - c_3^2)^2 + 4(c_3 - \alpha)^2(3\ell_{12}c_3 - (c_3^2 + c_3\alpha + \alpha^2))}}{2(c_3 - \alpha)^2}$$
$$\tag{C.5}$$

The function $g_{\mathcal{V}}$ is well defined, positive and decreasing on $[0, f_{\mathcal{V}}^{12}(c_3)]$. It verifies the identities $g_{\mathcal{V}}(0) = f_{\mathcal{V}}^{23}(c_1)$ and $g_{\mathcal{V}}(f_{\mathcal{V}}^{12}(c_3)) = 0$. We also introduce $h_{\mathcal{V}}^{13}$ as:

$$h_{\mathcal{V}}^{13}(\alpha) = c_1 \frac{2\alpha^3 + 3(c_3 - \alpha)(c_3(c_3 - \ell_{12}) + \ell_{12}\alpha) - \sqrt{3(c_3 - \alpha)^2(3(c_3(c_3 - \ell_{12}) + \ell_{12}\alpha)^2 + 4(c_3 - \ell_{12})\alpha^3)}}{2\alpha(\alpha^2 + 3c_3(c_3 - \alpha))}$$
$$\tag{C.6}$$

The function $h_{\mathcal{V}}^{13}$ is well defined, positive and monotonically increasing on $[0, c_3]$. It verifies the identities $h_{\mathcal{V}}^{13}(0) = 0$ and $h_{\mathcal{V}}^{13}(c_3) = c_1$. The angles of the local chart of figure 5 are given by:

$$\theta_1 = \arctan\left(\frac{\ell_{23}}{c_2}\right) \quad \theta_2^{\mathrm{t}} = \arctan\left(\frac{3\ell_{23}}{c_2}\right) \quad \theta_3 = \arctan\left(\frac{c_1}{c_2}\right) \quad \theta_4^{\mathrm{t}} = \arctan\left(\frac{c_1}{3\ell_{13}}\right) \quad \theta_5 = \arctan\left(\frac{c_1}{\ell_{13}}\right)$$

$$\theta_2^{\mathrm{h}} = \arctan\left(\frac{c_1 - f_{\mathcal{V}}^{23}(c_1)}{c_2}\right) \qquad \theta_4^{\mathrm{h}} = \arctan\left(\frac{c_1}{c_2 - f_{\mathcal{V}}^{13}(c_2)}\right)$$

Consider the third-degree polynomial $x^3 + px + q = 0$. When the discriminant $\Delta = 4p^3 + 27q^2 \le 0$, the polynomial has three real roots given by ($k \in \{0, 1, 2\}$):

$$x_k = 2\sqrt{\frac{-p}{3}} \cos\left(\frac{1}{3}\arccos\left(\frac{-q}{2\sqrt{\left(-\frac{p}{3}\right)^3}}\right) + \frac{2k\pi}{3}\right) \tag{C.7}$$

*Appendix C.2. Parametrization of the* `Triangle` *configuration*
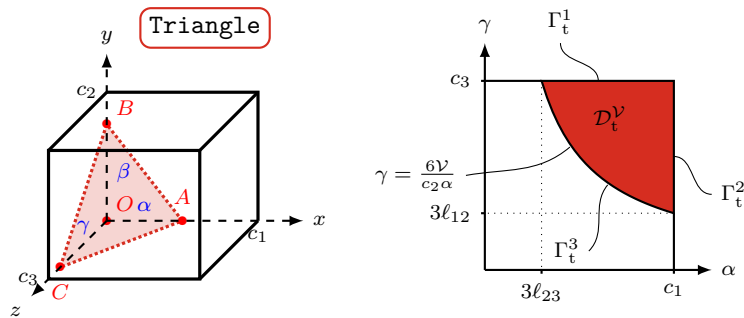*Appendix C.2.1. Parametrization in* $(\alpha, \gamma)$



Figure C.12: `Triangle` configuration (left) and definition domain $\mathcal{D}_{\mathrm{t}}^{\mathcal{V}}$ with $\chi < \frac{1}{6}$ (right).

21

In the `Triangle` configuration, the plane — the surface $\mathfrak{P}$ defined in (C.2) — intersects the cell as presented on the left of figure C.12. The coordinates of the points are given by $A = (\alpha, 0, 0)$, $B = (0, \beta, 0)$, and $C = (0, 0, \gamma)$. The coefficients of the plane (C.2) are given by:

$$a_1 = \frac{1}{\alpha} \qquad a_2 = \frac{1}{\beta} \qquad a_3 = \frac{1}{\gamma} \tag{C.8}$$

The volume of the tetrahedron $OABC$ is given by $\mathcal{V}_{\mathrm{t}}(\alpha, \beta, \gamma) = \frac{\alpha\beta\gamma}{6}$. Its centroid is given by $\mathcal{C}_{\mathrm{t}}(\alpha, \beta, \gamma) = \frac{1}{4}[\alpha, \beta, \gamma]$. By imposing the fixed reference volume $\mathcal{V}$, we obtain:

$$\beta_{\mathrm{t}}(\alpha, \gamma, \mathcal{V}) = \frac{6\mathcal{V}}{\alpha\gamma} \qquad \mathcal{C}_{\mathrm{t}}^{\mathcal{V}}(\alpha, \gamma) = \frac{1}{4}\left[\alpha, \frac{6\mathcal{V}}{\alpha\gamma}, \gamma\right] \tag{C.9}$$

In closed form, the centroid verifies the equation $Y = \frac{3\mathcal{V}}{32XZ}$ which is a portion of a hyperboloid. When the parameters $\alpha \in [0, c_1]$ and $\gamma \in [0, c_3]$ are fixed, we have $\beta_{\mathrm{t}} \in [0, c_2]$, so, $0 \le \frac{6\mathcal{V}}{\alpha\gamma} \le c_2$. The domain $\mathcal{D}_{\mathrm{t}}^{\mathcal{V}}$, represented on figure C.12, is given by:

$$\mathcal{D}_{\mathrm{t}}^{\mathcal{V}} = \left\{ (\alpha, \gamma) \in [0, c_1] \times [0, c_3] \;\middle|\; \gamma \ge \frac{6\mathcal{V}}{c_2\alpha} \right\}$$

Its three limit curves are given by $\Gamma_{\mathrm{t}}^3 \colon \alpha \mapsto \left(\alpha, \frac{6\mathcal{V}}{c_2\alpha}\right)$ with $\alpha \in [3\ell_{23}, c_1]$, $\Gamma_{\mathrm{t}}^2 \colon \gamma \mapsto (c_1, \gamma)$ with $\gamma \in [3\ell_{12}, c_3]$ and $\Gamma_{\mathrm{t}}^1 \colon \alpha \mapsto (\alpha, c_3)$ with $\alpha \in [3\ell_{23}, c_1]$.

*Appendix C.2.2. Parametrization of the centroid and the limit curves in $(\theta, \phi)$*

From equations (C.3), (C.8) and relation (C.9), we get $\tan(\theta) = \frac{\alpha}{\beta} = \frac{\alpha^2\gamma}{6\mathcal{V}}$ and $\cot(\phi) = \frac{\alpha}{\gamma}\cos(\theta)$. We solve these equations for $\alpha$ and $\gamma$ to obtain:

$$\gamma_{\mathrm{t}}(\theta, \phi, \mathcal{V}) = \left(\frac{6\mathcal{V}\tan(\theta)}{(\cot(\phi)\sec(\theta))^2}\right)^{\frac{1}{3}} \qquad \alpha_{\mathrm{t}}(\theta, \phi, \mathcal{V}) = \gamma_{\mathrm{t}}(\theta, \phi, \mathcal{V})\cot(\phi)\sec(\theta) \tag{C.10}$$

We obtain the final parametrization (16) by replacing $\alpha$ and $\gamma$ in (C.9) by their expression given in (C.10).

The limit curves in $(\theta, \phi)$ are obtained from the limit curves in $(\alpha, \gamma)$. For the curve $\Gamma_{\mathrm{t}}^3$, we have $\gamma = \frac{6\mathcal{V}}{c_2\alpha}$. Hence, $\tan(\theta) = \frac{\alpha}{c_2}$ and $\cot(\phi) = \frac{c_2\alpha^2}{6\mathcal{V}}\cos(\theta)$. When solved for $(\theta, \phi)$, we obtain $\phi_{\mathrm{t}3}^{\lim}(\theta)$ (12) defined on $[\theta_2^{\mathrm{t}}, \theta_3]$. For the curve $\Gamma_{\mathrm{t}}^2$, we have $\alpha = c_1$. Hence, $\tan(\theta) = \frac{c_1^2\gamma}{6\mathcal{V}}$ and $\cot(\phi) = \frac{c_1}{\gamma}\cos(\theta)$. We obtain $\phi_{\mathrm{t}2}^{\lim}(\theta)$ (12) defined on $[\theta_3, \theta_4^{\mathrm{t}}]$. For the curve $\Gamma_{\mathrm{t}}^1$, we have $\gamma = c_3$. Hence, $\tan(\theta) = \frac{c_3\alpha^2}{6\mathcal{V}}$ and $\cot(\phi) = \frac{\alpha}{c_3}\cos(\theta)$. We obtain $\phi_{\mathrm{t}1}^{\lim}(\theta)$ (12) defined on $[\theta_2^{\mathrm{t}}, \theta_4^{\mathrm{t}}]$.

*Appendix C.3. Parametrization of the `QuadFace` configuration*

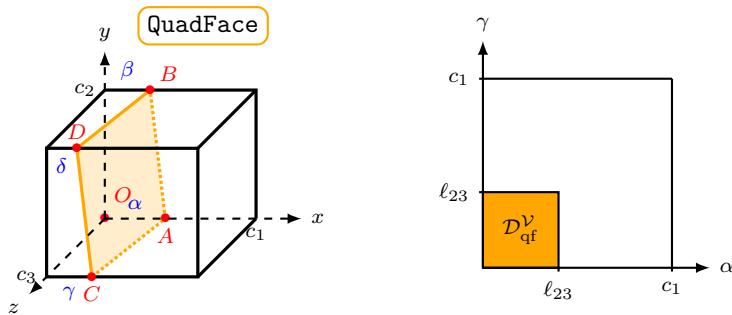*Appendix C.3.1. Parametrization in $(\alpha, \gamma)$*



Figure C.13: `QuadFace` configuration (left) and definition domain $\mathcal{D}_{\mathrm{qf}}^{\mathcal{V}}$ (right).

In the `QuadFace` configuration, the plane intersects the cell as presented on the left of figure C.13. The coordinates of the points are given by $A = (\alpha, 0, 0)$, $B = (\beta, c_2, 0)$, $C = (\gamma, 0, c_3)$, and $D = (\delta, c_2, c_3)$. The coefficients of the plane (C.2) are given by:

$$a_1 = \frac{1}{\alpha} \qquad a_2 = \frac{\alpha - \beta}{c_2 \alpha} \qquad a_3 = \frac{\alpha - \gamma}{c_3 \alpha} \tag{C.11}$$

Since the point $D$ belongs to the plane, we have $\delta = \beta + \gamma - \alpha$. The plane can be parametrized by $x = \zeta_{\mathrm{qf}}(y, z) = \alpha + \frac{\beta - \alpha}{c_2} y + \frac{\gamma - \alpha}{c_3} z$. The volume of the approximation is given by:

$$\mathcal{V}_{\mathrm{qf}}(\alpha, \beta, \gamma) = \int_0^{c_3} \int_0^{c_2} \int_0^{\zeta_{\mathrm{qf}}(y,z)} 1 \, \mathrm{d}x \, \mathrm{d}y \, \mathrm{d}z = \frac{c_2 c_3 (\beta + \gamma)}{2} \tag{C.12}$$

The centroid of the approximation is given by:

$$\mathcal{C}_{\mathrm{qf}}(\alpha, \beta, \gamma) = \frac{1}{\mathcal{V}_{\mathrm{qf}}(\alpha, \beta, \gamma)} \int_0^{c_3} \int_0^{c_2} \int_0^{\zeta_{\mathrm{qf}}(y,z)} \begin{bmatrix} x \\ y \\ z \end{bmatrix} \mathrm{d}x \, \mathrm{d}y \, \mathrm{d}z = \frac{1}{6(\beta + \gamma)} \begin{bmatrix} 2\gamma^2 + 3\beta\gamma + 2\beta^2 - \alpha(\beta + \gamma) + \alpha^2 \\ c_2(3\gamma + 4\beta - \alpha) \\ c_3(4\gamma + 3\beta - \alpha) \end{bmatrix}$$

By imposing the fixed reference volume $\mathcal{V}$ in (C.12), we obtain:

$$\beta_{\mathrm{qf}}(\alpha, \gamma, \mathcal{V}) = \ell_{23} - \gamma \qquad \mathcal{C}_{\mathrm{qf}}^{\mathcal{V}}(\alpha, \gamma) = \frac{1}{6\ell_{23}} \begin{bmatrix} 2(\ell_{23})^2 - \ell_{23}(\alpha + \gamma) + \alpha^2 + \gamma^2 \\ c_2(4\ell_{23} - (\alpha + \gamma)) \\ c_3(3\ell_{23} - (\alpha - \gamma)) \end{bmatrix} \tag{C.13}$$

In closed form, the centroid verifies the equation $X = \frac{\mathcal{V}}{2c_2^3 c_3^3} \left( 12 c_3^2 (Y - \frac{c_2}{2})^2 + 12 c_2^2 (Z - \frac{c_3}{2})^2 + c_2^2 c_3^2 \right)$ which is a portion of a paraboloid. When the parameters $\alpha, \gamma \in [0, c_1]$ are fixed, we have $\beta_{\mathrm{qf}}, \delta_{\mathrm{qf}} \in [0, c_1]$, so $0 \leq \ell_{23} - \gamma \leq c_1$ and $0 \leq \ell_{23} - \alpha \leq c_1$. Hence, using the relation $\ell_{23} \leq c_1$ (as $\mathcal{V} \leq c_1 c_2 c_3 / 2$), we get $(\alpha, \gamma) \in [0, \ell_{23}]^2$. The definition domain $\mathcal{D}_{\mathrm{qf}}^{\mathcal{V}}$, represented on figure C.13, is then given by:

$$\mathcal{D}_{\mathrm{qf}}^{\mathcal{V}} = \left\{ (\alpha, \gamma) \in [0, c_1]^2 \mid \gamma \leq \ell_{23} \text{ and } \alpha \leq \ell_{23} \right\}$$

*Appendix C.3.2. Parametrization in $(\theta, \phi)$ of the centroid*

From (C.3), (C.11) and relation (C.13), we obtain $\tan(\theta) = \frac{\alpha - \beta}{c_2} = \frac{\alpha + \gamma - \ell_{23}}{c_2}$ and $\cot(\phi) = \frac{\alpha - \gamma}{c_3} \cos(\theta)$. We solve these equations for $\alpha$ and $\gamma$ to obtain the following relations:

$$\gamma_{\mathrm{qf}}(\theta, \phi, \mathcal{V}) = \frac{1}{2} \left( c_2 \tan(\theta) + \ell_{23} - c_3 \cot(\phi) \sec(\theta) \right) \qquad \alpha_{\mathrm{qf}}(\theta, \phi, \mathcal{V}) = \gamma_{\mathrm{qf}}(\theta, \phi, \mathcal{V}) + c_3 \cot(\phi) \sec(\theta) \tag{C.14}$$

After simplifications, we obtain the final parametrization (17) by replacing $\alpha$ and $\gamma$ in (C.13) with their expression given in (C.14). For the limit curves, we will use those given by the `Penta` configuration.

*Appendix C.4. Parametrization of the `QuadEdge` configuration*

*Appendix C.4.1. Parametrization in $(\alpha, \gamma)$*

In the `QuadEdge` configuration, the plane intersects the cell as presented on figure C.14. The coordinates of the points are given by $A = (\alpha, 0, 0)$, $B = (0, \beta, 0)$, $C = (\gamma, 0, c_3)$, and $D = (0, \delta, c_3)$. The coefficients of the plane (C.2) are given by:

$$a_1 = \frac{1}{\alpha} \qquad a_2 = \frac{1}{\beta} \qquad a_3 = \frac{\alpha - \gamma}{c_3 \alpha} \tag{C.15}$$
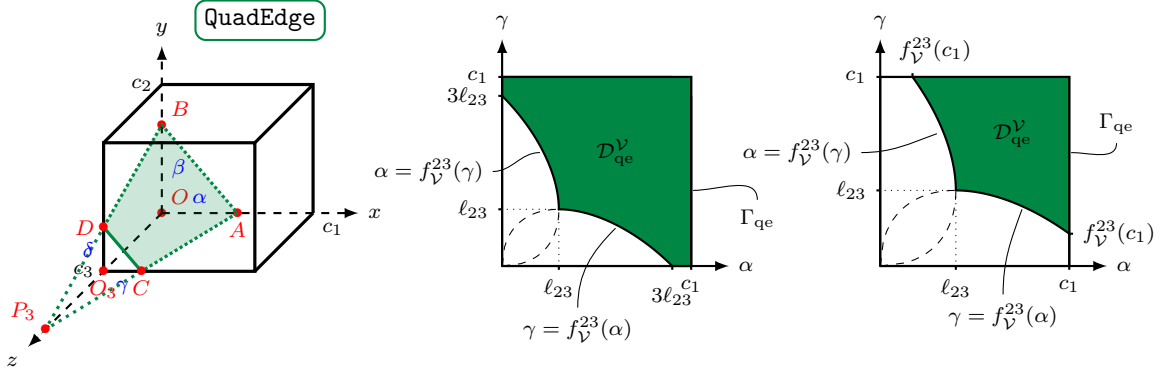
Figure C.14: `QuadEdge` configuration (left), definition domain $\mathcal{D}_{\text{qe}}^{\mathcal{V}}$ for $\chi < \frac{1}{6}$ (middle) and for $\chi > \frac{1}{6}$ (right).

Since point $D$ belongs to plane $\mathfrak{P}$, we have $\delta = \frac{\beta\gamma}{\alpha}$. We introduce the points $O_3 = (0, 0, c_3)$ and $P_3 = (0, 0, h_3)$ where $h_3 = \frac{c_3\alpha}{\alpha-\gamma}$. The last point corresponds to the intersection of the planes $\{x = 0\}$, $\{y = 0\}$, and the interface. The volume and the centroid of the domain $OABO_3CD$ are computed using the additivity of the volume and the first momentum of the tetrahedrons $OABP_3$ and $O_3CDP_3$, which gives:

$$\mathcal{V}_{\text{qe}}(\alpha, \beta, \gamma) = \frac{c_3\beta(\alpha^2 + \alpha\gamma + \gamma^2)}{6\alpha} \qquad \mathcal{C}_{\text{qe}}(\alpha, \beta, \gamma) = \begin{bmatrix} \frac{\alpha^3 + \alpha^2\gamma + \alpha\gamma^2 + \gamma^3}{4(\alpha^2 + \alpha\gamma + \gamma^2)} \\ \frac{\beta(\alpha^3 + \alpha^2\gamma + \alpha\gamma^2 + \gamma^3)}{4\alpha(\alpha^2 + \alpha\gamma + \gamma^2)} \\ \frac{c_3(3\gamma^2 + 2\alpha\gamma + \alpha^2)}{4(\alpha^2 + \alpha\gamma + \gamma^2)} \end{bmatrix} \qquad \text{(C.16)}$$

Note that the volume and the centroid are continuous between the `QuadEdge` and the `Triangle` configurations since $\mathcal{V}_{\text{qe}}(\alpha, \beta, 0) = \mathcal{V}_{\text{t}}(\alpha, \beta, c_3)$ and $\mathcal{C}_{\text{qe}}(\alpha, \beta, 0) = \mathcal{C}_{\text{t}}(\alpha, \beta, c_3)$. By imposing a fixed reference volume $\mathcal{V}$ in (C.16), we get:

$$\beta_{\text{qe}}(\alpha, \gamma, \mathcal{V}) = \frac{6\mathcal{V}\alpha}{c_3(\alpha^2 + \alpha\gamma + \gamma^2)} \qquad \text{(C.17)}$$

When the parameters $\alpha$, $\gamma \in [0, c_1]$ are fixed, we have $\beta_{\text{qe}} \in [0, c_2]$ so $0 \leq \frac{6\mathcal{V}\alpha}{c_3(\alpha^2 + \alpha\gamma + \gamma^2)} \leq c_2$. The right inequality writes $\gamma^2 + \alpha\gamma + \alpha^2 - 3\ell_{23}\alpha \geq 0$ or equivalently $\gamma \geq f_{\mathcal{V}}^{23}(\alpha)$ using (C.4) where we keep the positive solution because $\gamma \geq 0$. We have also $\delta_{\text{qe}} \in [0, c_2]$ so $0 \leq \frac{6\mathcal{V}\gamma}{c_3(\alpha^2 + \alpha\gamma + \gamma^2)} \leq c_2$ and hence we obtained similarly that $\alpha \geq f_{\mathcal{V}}^{23}(\gamma)$. The definition domain $\mathcal{D}_{\text{qe}}^{\mathcal{V}}$ represented in figure C.14 is then given by:

$$\mathcal{D}_{\text{qe}}^{\mathcal{V}} = \left\{ (\alpha, \gamma) \in [0, c_1]^2 \mid \gamma \geq f_{\mathcal{V}}^{23}(\alpha) \text{ and } \alpha \geq f_{\mathcal{V}}^{23}(\gamma) \right\}$$

The limit curve $\Gamma_{\text{qe}} \colon \gamma \mapsto (c_1, \gamma)$ is defined for $\gamma \in [0, c_1]$ if $\chi < \frac{1}{6}$ and for $\gamma \in [f_{\mathcal{V}}^{23}(c_1), c_1]$ if $\chi > \frac{1}{6}$.

*Appendix C.4.2. Parametrization of the centroid and the limit curves in $(\theta, \phi)$*

From equations (C.3), (C.15) and relation (C.17), we get $\tan(\theta) = \frac{\alpha}{\beta} = \frac{c_3(\alpha^2 + \alpha\gamma + \gamma^2)}{6\mathcal{V}}$ and $\cot(\phi) = \frac{\alpha-\gamma}{c_3}\cos(\theta)$. We obtain a second degree polynomial equation in $\gamma$ and we get the following relations — keeping the positive root — with $T_2 = c_2\tan(\theta)$ and $T_3 = c_3\cot(\phi)\sec(\theta)$:

$$\gamma_{\text{qe}}(\theta, \phi, \mathcal{V}) = \frac{1}{6}\left(-3T_3 + \sqrt{36\ell_{23}T_2 - 3(T_3)^2}\right) \qquad \alpha_{\text{qe}}(\theta, \phi, \mathcal{V}) = \gamma_{\text{qe}}(\theta, \phi, \mathcal{V}) + T_3 \qquad \text{(C.18)}$$

After simplifications, we obtain the final parametrization (18) by replacing $\alpha$, $\beta$, and $\gamma$ in (C.16) by their expressions given in (C.17) and (C.18).

The limit curves in $(\theta, \phi)$ are obtained from the limit curves in $(\alpha, \gamma)$. For the curve $\Gamma_{\text{qe}}$, we have $\alpha = c_1$. Hence, $\tan(\theta) = \frac{c_3(c_1^2 + c_1\gamma + \gamma^2)}{6\mathcal{V}}$ and $\cot(\phi) = \frac{c_1-\gamma}{c_3}\cos(\theta)$. By solving the second order equation in $\gamma$ and keeping the positive root, we obtain $\phi_{\text{qe}}^{\lim}(\theta)$ (14a) defined on $[\theta_4^t, \theta_5]$. If $\chi > \frac{1}{6}$, we have $\gamma \in [f_{\mathcal{V}}^{23}(c_1), c_1]$. Hence, $\phi_{\text{qe}}^{\lim}(\theta)$ is defined on $[\theta_3, \theta_5]$. For the curve $\Gamma_{\text{rot}}$, we obtain in similar way $\phi_{\text{rot}}^{\lim}(\theta)$ (14b) defined on $[\theta_3, \theta_6]$. If $\chi > \frac{1}{6}$, $\alpha$ belongs to $[\ell_{12}, c_3]$. Hence, $\phi_{\text{rot}}^{\lim}(\theta)$ is defined on $[\theta_4^h, \theta_6]$.

24

*Appendix C.5. Parametrization of the* `Penta` *configuration*

*Appendix C.5.1. Parametrization in* $(\alpha, \gamma)$
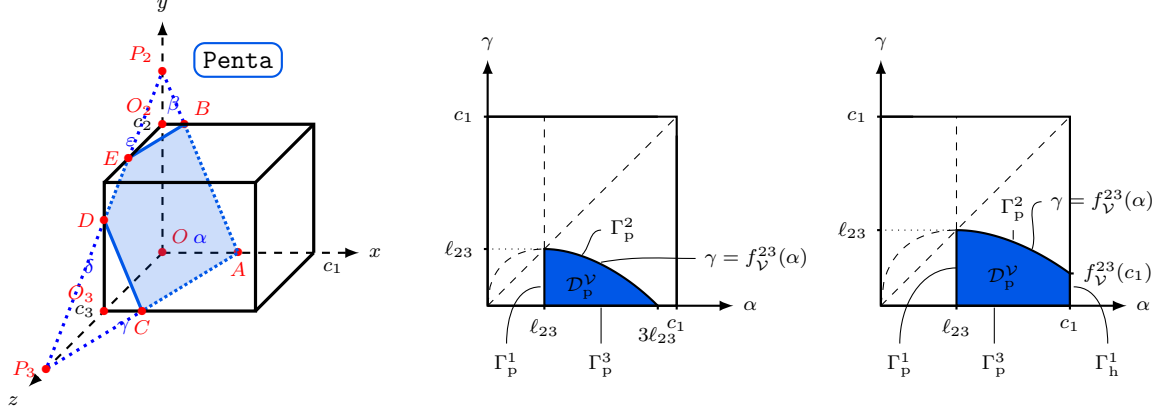


Figure C.15: `Penta` configuration (left), definition domain $\mathcal{D}_{\mathrm{p}}^{\mathcal{V}}$ with $\chi < \frac{1}{6}$ (middle) and $\chi > \frac{1}{6}$ (right).

In the `Penta` configuration, the plane intersects the cell as presented on the left of figure C.15. The coordinates of the points are given by $A = (\alpha, 0, 0)$, $B = (\beta, c_2, 0)$, $C = (\gamma, 0, c_3), D = (0, \delta, c_3)$, and $E = (0, c_2, \varepsilon)$. The coefficients of the plane (C.2) are given by:

$$a_1 = \frac{1}{\alpha} \qquad a_2 = \frac{\alpha - \beta}{c_2 \alpha} \qquad a_3 = \frac{\alpha - \gamma}{c_3 \alpha} \tag{C.19}$$

Since the points $D$ and $E$ belong to the plane, we have $\delta = \frac{c_2 \gamma}{\alpha - \beta}$ and $\varepsilon = \frac{c_3 \beta}{\alpha - \gamma}$. Furthermore, we have $\alpha, \beta, \gamma \in [0, c_1]$. $\delta \in [0, c_2]$, $\varepsilon \in [0, c_3]$, thus $0 \le \frac{c_2 \gamma}{\alpha - \beta} \le c_2$. The left inequality is satisfied if $\alpha \ge \beta$ and the right one is satisfied if $\alpha \ge \beta + \gamma$. We also have $0 \le \frac{c_3 \beta}{\alpha - \gamma} \le c_3$. The left inequality is satisfied if $\alpha \ge \gamma$ and the right one is satisfied if $\alpha \ge \beta + \gamma$. Therefore, only one inequality stands:

$$\beta \le \alpha - \gamma \tag{C.20}$$

We introduce the points $O_3 = (0, 0, c_3), O_2 = (0, c_2, 0)$, and $P_2 = (0, h_2, 0)$ where $h_2 = \frac{c_2 \alpha}{\alpha - \beta}$. The point $P_2$ is the intersection of the planes $\{x = 0\}$, $\{z = 0\}$ and the interface $\mathfrak{P}$. We also introduce the point $P_3 = (0, 0, h_3)$ where $h_3 = \frac{c_3 \alpha}{\alpha - \gamma}$ as the intersection of the planes $\{x = 0\}$, $\{y = 0\}$ and the interface $\mathfrak{P}$. The volume and the centroid of the domain $OABO_2EDCO_3$ are computed using the additivity of the volume and the first momentum of the tetrahedrons $OAP_2P_3$, $O_2BEP_2$ and $O_3CDP_3$, so:

$$\mathcal{V}_{\mathrm{p}}(\alpha, \beta, \gamma) = \frac{c_2 c_3 (\alpha^3 - (\beta^3 + \gamma^3))}{6(\alpha - \beta)(\alpha - \gamma)} \qquad \mathcal{C}_{\mathrm{p}}(\alpha, \beta, \gamma) = \begin{bmatrix} \frac{\alpha^4 - (\beta^4 + \gamma^4)}{4(\alpha^3 - (\beta^3 + \gamma^3))} \\ \frac{c_2(\alpha^4 - (\beta^4 + \gamma^4) - 4\beta^3(\alpha - \beta))}{4(\alpha - \beta)(\alpha^3 - (\beta^3 + \gamma^3))} \\ \frac{c_3(\alpha^4 - (\beta^4 + \gamma^4) - 4\gamma^3(\alpha - \gamma))}{4(\alpha - \gamma)(\alpha^3 - (\beta^3 + \gamma^3))} \end{bmatrix} \tag{C.21}$$

Note that the volume and the centroid are continuous between the `QuadEdge` and the `Penta` configurations since $\beta_{\mathrm{p}} = 0$ is equivalent to $\beta_{\mathrm{qe}} = c_2$ and we verify that $\mathcal{V}_{\mathrm{p}}(\alpha, 0, \gamma) = \mathcal{V}_{\mathrm{qe}}(\alpha, c_2, \gamma)$ and $\mathcal{C}_{\mathrm{p}}(\alpha, 0, \gamma) = \mathcal{C}_{\mathrm{qe}}(\alpha, c_2, \gamma)$. Similarly, the volume and the centroid are continuous between the `QuadEdge` and the `QuadFace` configurations since $\delta_{\mathrm{qf}} = \beta + \gamma - \alpha = 0$ is equivalent to $\delta_{\mathrm{p}} = \frac{c_2 \gamma}{\alpha - \beta} = c_2$, that is $\beta_{\mathrm{p}} = \beta_{\mathrm{qf}} = \alpha - \gamma$, and by verifying that $\mathcal{V}_{\mathrm{p}}(\alpha, \alpha - \gamma, \gamma) = \mathcal{V}_{\mathrm{qf}}(\alpha, \alpha - \gamma, \gamma)$ and $\mathcal{C}_{\mathrm{p}}(\alpha, \alpha - \gamma, \gamma) = \mathcal{C}_{\mathrm{qf}}(\alpha, \alpha - \gamma, \gamma)$.

For a given reference fixed volume we get with (C.21) that $\beta$ is the root of the following third degree polynomial:

$$\Psi_{\mathrm{p}}(\alpha, \beta, \gamma) = \beta^3 - 3\ell_{23}(\alpha - \gamma)\beta - (\alpha - \gamma)\left(\alpha^2 + \alpha\gamma + \gamma^2 - 3\ell_{23}\alpha\right) = 0 \tag{C.22}$$

25

Let us find the definition domain of the `Penta` configuration:

$$\mathcal{D}_p^{\mathcal{V}} = \left\{ (\alpha, \gamma) \in [0, c_1]^2 \mid 0 \le \beta_p(\alpha, \gamma, \mathcal{V}) \le c_1 \text{ and } \beta_p(\alpha, \gamma, \mathcal{V}) \le \alpha - \gamma \right\}$$

where $\beta_p(\alpha, \gamma, \mathcal{V})$ is solution of (C.22). To find this domain, let us first find its boundaries. If $\beta = c_1$, we have $c_1 \ge \alpha \ge c_1 + \gamma$ and therefore $(\alpha, \gamma) = (c_1, 0)$. With (C.22) and using (C.4) we have:

$$\text{For } \beta = 0 \qquad \Psi_p(\alpha, 0, \gamma) = \left(\gamma - \alpha\right)\left(\gamma - f_{\mathcal{V}}^{23}(\alpha)\right)\left(\gamma - \tilde{f}_{\mathcal{V}}^{23}(\alpha)\right) = 0 \qquad \text{(C.23)}$$

$$\text{For } \beta = \alpha - \gamma \qquad \Psi_p(\alpha, \alpha - \gamma, \gamma) = 3\gamma(\alpha - \gamma)(\ell_{23} - \alpha) = 0 \qquad \text{(C.24)}$$

Therefore, the possible boundaries of the domain $\mathcal{D}_p^{\mathcal{V}}$ are necessary in the following list: $\alpha = 0$, $\alpha = c_1$, $\gamma = 0$, $\gamma = c_1$, $\gamma = \alpha$, $\gamma = f_{\mathcal{V}}^{23}(\alpha)$, or $\alpha = \ell_{23}$. The root $\gamma = \tilde{f}_{\mathcal{V}}^{23}(\alpha)$ is excluded since it is negative, so outside of $[0, c_1]^2$. These curves partition $[0, c_1]^2$ in six regions as represented in figure C.15. Thus $\mathcal{D}_p^{\mathcal{V}}$ is the reunion of some — possibly only one — of these regions. It is easy to check numerically by picking one value in these regions that five of them do not verify all the constraints. In each of these regions, the three roots of (C.22) verifies either $\beta \in \mathbb{C}$ or $\beta < 0$ or $\beta > \alpha - \gamma$, which violates the conditions. Therefore the definition domain of the `Penta` is necessarily given by the remaining region:

$$\mathcal{D}_p^{\mathcal{V}} = \left\{ (\alpha, \gamma) \in [0, c_1]^2 \mid \alpha \ge \ell_{23} \text{ and } \gamma \le f_{\mathcal{V}}^{23}(\alpha) \right\}$$

The limit curves are given by $\Gamma_p^1 \colon \alpha \mapsto (\ell_{23}, \gamma)$ where $\gamma \in [0, \ell_{23}]$, $\Gamma_p^2 \colon \alpha \mapsto (\alpha, f_{\mathcal{V}}^{23}(\alpha))$ where $\alpha \in [\ell_{23}, \min(3\ell_{23}, c_1)]$ and $\Gamma_p^3 \colon \alpha \mapsto (\alpha, 0)$ where $\alpha \in [\ell_{23}, \min(3\ell_{23}, c_1)]$. When $\chi > \frac{1}{6}$, there is another curve $\Gamma_h^1 \colon \gamma \mapsto (c_1, \gamma)$ common to the `Hexa` configuration where $\gamma \in [0, f_{\mathcal{V}}^{23}(c_1)]$.

In Appendix C.7.2, we have proved that the discriminant of the third-degree equation (C.22) is negative on $\mathcal{D}_p^{\mathcal{V}}$, so there are three real roots $\beta_k$ for $k \in [\![0, 2]\!]$ that can be expressed by formula (C.7). In Appendix C.7.2, we have also shown that the only solution that verifies $0 \le \beta \le \alpha - \gamma$ on $\mathcal{D}_p^{\mathcal{V}}$ is the root for $k = 2$ given by:

$$\beta_p(\alpha, \gamma, \mathcal{V}) = 2\sqrt{\ell_{23}(\alpha - \gamma)} \cos\left(\frac{1}{3} \arccos\left(\frac{\alpha^2 + \alpha\gamma + \gamma^2 - 3\ell_{23}\alpha}{2\ell_{23}\sqrt{\ell_{23}(\alpha - \gamma)}}\right) + \frac{4\pi}{3}\right) \qquad \text{(C.25)}$$

In the `Penta` configuration, we can find the following simpler formulas for the limits $\Gamma_p^1$, $\Gamma_p^2$ and $\Gamma_p^3$:

$$
\begin{aligned}
&\text{For } \Gamma_p^1 &&\forall \gamma \in [0, \ell_{23}], &&\beta_p(\ell_{23}, \gamma, \mathcal{V}) = \ell_{23} - \gamma \\
&\text{For } \Gamma_p^2 &&\forall \alpha \in [\ell_{23}, \min(3\ell_{23}, c_1)], &&\beta_p(\alpha, f_{\mathcal{V}}^{23}(\alpha), \mathcal{V}) = 0 \\
&\text{For } \Gamma_p^3 &&\forall \alpha \in [\ell_{23}, \min(3\ell_{23}, c_1)], &&\beta_p(\alpha, 0, \mathcal{V}) = f_{\mathcal{V}}^{23}(\alpha)
\end{aligned}
\qquad \text{(C.26)}
$$

When $\chi > \frac{1}{6}$, we did not find a simpler expression of the fourth limit $\Gamma_h^1$.

To obtain these formulas, we insert the equations of the limits into equation (C.22):

$$\text{On } \Gamma_p^1 \qquad \Psi_p(\ell_{23}, \beta, \gamma) = \left(\beta - f_{\mathcal{V}}^{23}(\ell_{23} - \gamma)\right)\left(\beta - \tilde{f}_{\mathcal{V}}^{23}(\ell_{23} - \gamma)\right)\left(\beta - (\ell_{23} - \gamma)\right) \qquad \text{(C.27)}$$

$$\text{On } \Gamma_p^2 \qquad \Psi_p(\alpha, \beta, f_{\mathcal{V}}^{23}(\alpha)) = \left(\beta - \sqrt{3\ell_{23}(\alpha - f_{\mathcal{V}}^{23}(\alpha))}\right)\left(\beta + \sqrt{3\ell_{23}(\alpha - f_{\mathcal{V}}^{23}(\alpha))}\right)\left(\beta - 0\right) \qquad \text{(C.28)}$$

$$\text{On } \Gamma_p^3 \qquad \Psi_p(\alpha, \beta, 0) = \left(\beta - \alpha\right)\left(\beta - \tilde{f}_{\mathcal{V}}^{23}(\alpha)\right)\left(\beta - f_{\mathcal{V}}^{23}(\alpha)\right) \qquad \text{(C.29)}$$

On each boundaries, there are three roots for $\beta$. It can proved by a direct computation that the first root of each expression corresponds to the root $k = 0$ of (C.22). The second term in each expression is negative since $\tilde{f}_{\mathcal{V}}^{23} < 0$, so it corresponds to the root $k = 1$ which is always negative as proved in proposition 1. Therefore the third term in each expression is the root $k = 2$ that we are looking for.

*Appendix C.5.2. Parametrization of the centroid and the limit curves in $(\theta, \phi)$*

From equations (C.3) and (C.19), we get $\tan(\theta) = \frac{\alpha - \beta}{c_2}$ and $\cot(\phi) = \frac{\alpha - \gamma}{c_3} \cos(\theta)$. These non-linear equations are difficult to solve directly because of the expression of $\beta$ in (C.25). Instead, we express $\alpha$ and $\gamma$ as a function of $\beta$, $\theta$, and $\phi$ to obtain a third degree polynomial on $\beta$ using the expression of the volume (C.21). We introduce the following notations:

$$\alpha = \beta + T_2 \quad \gamma = \beta + T_2 - T_3 \qquad \text{where} \qquad T_2 = c_2 \tan(\theta) \quad T_3 = c_3 \cot(\phi) \sec(\theta) \tag{C.30}$$

We replace these expressions in (C.21) to obtain the following third degree polynomial equation on $\beta$:

$$(\beta - T_3)^3 - 6T_2 T_3 (\beta - T_3) - 3T_2 T_3 (T_2 + T_3 - \ell_{23}) = 0 \tag{C.31}$$

We already know that the three roots are real. To find the suitable root, we can extend the proposition 1 to the case where $0 \leq X \leq 1$. In this case, $\beta_0 \geq 0$ and $\beta_1, \beta_2 \leq 0$. Note that we have to compute the lines $\{Y = -\frac{1}{2}\}$ and $\{\Psi = 0\}$ which are crucial for the inequalities. Using this extended proposition with $\mathcal{K} = 0$, $\mathcal{K} = c_1$ and $\mathcal{K} = \alpha - \gamma$, we can show that the only solution that verifies $\beta \leq \alpha - \gamma$, $0 \leq \alpha \leq c_1$, $0 \leq \beta \leq c_1$, and $0 \leq \gamma \leq c_1$ is given by the root $k = 2$. The root can be expressed by:

$$\beta_p(\theta, \phi, \mathcal{V}) = T_3 + 2\sqrt{2T_2 T_3} \mathcal{X}_p \qquad \mathcal{X}_p = \cos\left(\frac{1}{3} \arccos\left(\frac{3(T_2 + T_3 - \ell_{23})}{4\sqrt{2T_2 T_3}}\right) + \frac{4\pi}{3}\right) \tag{C.32}$$

where $\mathcal{X}_p$ verifies the following equation:

$$(\mathcal{X}_p)^3 - \frac{3}{4}\mathcal{X}_p - \frac{3(T_2 + T_3 - \ell_{23})}{16\sqrt{2T_2 T_3}} = 0 \tag{C.33}$$

To obtain the final parametrization (19), we replace $\alpha$, $\beta$ and $\gamma$ in (C.21) by their expressions given in (C.30) and (C.32). We obtain a fourth degree polynomial in $\mathcal{X}_p$ for each component. Then we use equation (C.33) to get a second degree polynomial in each component. Finally, after some simplifications, we obtain equation (19).

For the limit curve $\Gamma_p^1$, $\alpha = \ell_{23}$ hence, with formulas (C.26), we have $c_2 \tan(\theta) = \ell_{23} - \beta_p(\ell_{23}, \gamma, \mathcal{V}) = \gamma$ and $c_3 \cot(\phi) = (\ell_{23} - \gamma) \cos(\theta)$. We obtain $\phi_{p1}^{\lim}(\theta)$ (13a) defined on $[0, \theta_1]$. For the limit curve $\Gamma_p^2$, $\gamma = f_{\mathcal{V}}^{23}(\alpha)$ hence, with formulas (C.26), we have $c_2 \tan(\theta) = \alpha - \beta_p(\alpha, f_{\mathcal{V}}^{23}(\alpha), \mathcal{V}) = \alpha$ and $c_3 \cot(\phi) = (\alpha - f_{\mathcal{V}}^{23}(\alpha)) \cos(\theta)$. We obtain $\phi_{p2}^{\lim}(\theta)$ (13b) defined on $[\theta_1, \theta_2^t]$. If $\chi > \frac{1}{6}$, we have $\alpha \in [\ell_{23}, c_1]$. Hence $\phi_{p2}^{\lim}(\theta)$ is defined on $[\theta_1, \theta_3]$. For the limit curve $\Gamma_p^3$, we have $\gamma = 0$ hence, with equations (C.26), we have $c_2 \tan(\theta) = \alpha - \beta_p(\alpha, 0, \mathcal{V}) = \alpha - f_{\mathcal{V}}^{23}(\alpha)$ and $c_3 \cot(\phi) = \alpha \cos(\theta)$. The equation $\alpha - f_{\mathcal{V}}^{23}(\alpha) = T_2$ is a second degree polynomial in $\alpha$. We obtain the limit $\phi_{p3}^{\lim}(\theta)$ (13c) defined on $[0, \theta_2^t]$. If $\chi > \frac{1}{6}$, we have $\alpha \in [\ell_{23}, c_1]$. Hence $\phi_{p3}^{\lim}(\theta)$ is defined on $[0, \theta_2^h]$.

For the limit curve $\Gamma_h^1$, $\alpha = c_1$ hence, we have $c_2 \tan(\theta) = c_1 - \beta_p(c_1, \gamma, \mathcal{V})$ and $c_3 \cot(\phi) = (c_1 - \gamma) \cos(\theta)$. In order to find $\gamma$ as a function of $\theta$, we replace $\beta = c_1 - T_2$ and $\alpha = c_1$ in the formula of the volume (C.22) to obtain the following equation:

$$\gamma^3 - 3\ell_{23} T_2 \gamma + (c_1 - T_2)^3 - c_1^3 + 3c_1 \ell_{23} T_2 = 0$$

Using the property of symmetry $\Psi_p(\alpha, \beta, \gamma) = \Psi_p(\alpha, \gamma, \beta)$, the above formula writes $\Psi_p(c_1, c_1 - T_2, \gamma) = 0$. As previously, we take the root $k = 2$ to get $\gamma \leq \alpha - \beta$. Hence, after some simplifications, we obtain formula (15a) defined on $[\theta_2^h, \theta_3]$. Note that we have used the relations $\beta_p(c_1, 0, \mathcal{V}) = f_{\mathcal{V}}^{23}(c_1)$ and $\beta_p(c_1, f_{\mathcal{V}}^{23}(c_1), \mathcal{V}) = 0$ coming from (C.26).

For the limit curve $\Gamma_h^2$ we chose the points $(0, \alpha, 0)$, $(0, \beta, c_3)$ and $(c_1, \gamma, 0)$ to get $a_1 = \frac{\alpha - \gamma}{c_1 \alpha}$, $a_2 = \frac{1}{\alpha}$, $a_3 = \frac{\alpha - \beta}{c_3 \alpha}$ and the limit is on $(c_2, \gamma)$ with $\gamma \in [0, f_{\mathcal{V}}^{13}(c_2)]$. We have $\gamma = c_2 - T_1$ and $c_3 \cot(\phi) = (c_2 - \beta) \sin(\theta)$. In order to find $\beta$ as a function of $\theta$, we replace $\gamma = c_2 - T_1$ and $\alpha = c_2$ in the formula of the volume (C.22) where $\ell_{23}$ is replaced $\ell_{13}$ to obtain the following equation:

$$\beta^3 - 3\ell_{13} T_1 \beta + (c_2 - T_1)^3 - c_2^3 + 3c_2 \ell_{13} T_1 = 0$$

Hence we obtain formula (15b) defined on $[\theta_3, \theta_4^{\mathrm{h}}]$.

For $\Gamma_{\mathrm{h}}^3$ we chose the points $(0, 0, \alpha)$, $(c_1, 0, \beta)$ and $(0, c_2, \gamma)$ to get $a_1 = \frac{\alpha - \beta}{c_1 \alpha}$, $a_2 = \frac{\alpha - \gamma}{c_2 \alpha}$, $a_3 = \frac{1}{\alpha}$ and the limit is on $(c_3, \gamma)$ with $\gamma \in [0, f_{\mathcal{V}}^{12}(c_3)])$. We can prove that $T_2(c_3 - \beta) = c_1(c_3 - \gamma)$ and $\cot(\phi)\sec(\theta) = \frac{c_1}{c_3 - \beta}$. In order to find $\beta$ as a function of $\theta$, we replace $\gamma = c_3 + \frac{T_2}{c_1}(\beta - c_3)$ and $\alpha = c_3$ in the formula of the volume (C.22) where $\ell_{23}$ is replaced $\ell_{12}$ to obtain the following equation:

$$\left(\frac{1}{c_3 - \beta} - \frac{c_1 + T_2}{c_1 c_3}\right)^3 + 3T_2 \frac{\ell_{12} - 2c_3}{c_1 c_3^3}\left(\frac{1}{c_3 - \beta} - \frac{c_1 + T_2}{c_1 c_3}\right) + 3T_2 \frac{(\ell_{12} - c_3)(c_1 + T_2)}{c_1^2 c_3^4} = 0$$

Hence using $c_3 - \ell_{12} = \frac{c_3}{c_1}(c_1 - \ell_{23})$ we obtain equation (15c) defined on $[\theta_2^{\mathrm{h}}, \theta_4^{\mathrm{h}}]$.

*Appendix C.6. Parametrization of the* `Hexa` *configuration*

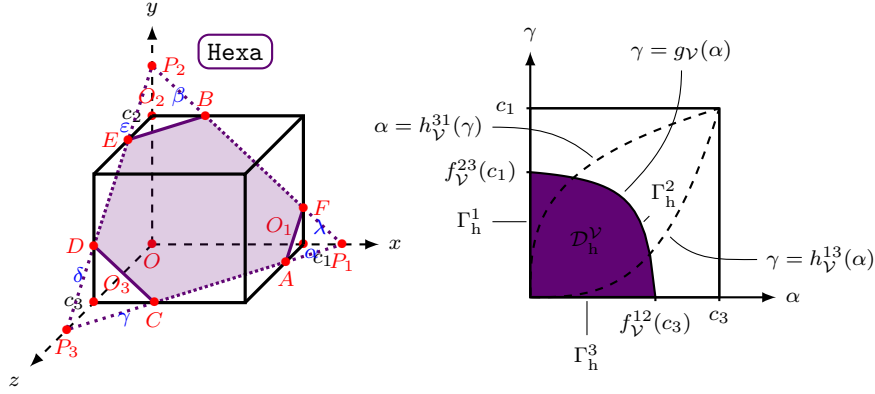*Appendix C.6.1. Parametrization in* $(\alpha, \gamma)$



Figure C.16: `Hexa` configuration (left) and definition domain $\mathcal{D}_h^{\mathcal{V}}$ with $\chi > \frac{1}{6}$ (right).

In the `Hexa` configuration, the plane intersects the cell as presented in figure C.16. The coordinates of the intersection points are given by $A = (c_1, 0, \alpha)$, $B = (\beta, c_2, 0)$, $C = (\gamma, 0, c_3)$, $D = (0, \delta, c_3)$, $E = (0, c_2, \varepsilon)$, and $F = (c_1, \lambda, 0)$. The coefficients of the plane (C.2) are given by:

$$a_1 = \frac{c_3 - \alpha}{c_1 c_3 - \alpha\gamma} \qquad a_2 = \frac{c_3(c_1 - \beta) + \alpha(\beta - \gamma)}{c_2(c_1 c_3 - \alpha\gamma)} \qquad a_3 = \frac{c_1 - \gamma}{c_1 c_3 - \alpha\gamma} \tag{C.34}$$

Since the points $D$, $E$, and $F$ belongs to the plane, $\delta = \frac{c_2\gamma(c_3 - \alpha)}{c_3(c_1 - \beta) + \alpha(\beta - \gamma)}$, $\varepsilon = \frac{\beta(c_3 - \alpha)}{c_1 - \gamma}$, and $\lambda = \frac{c_2\alpha(c_1 - \gamma)}{c_3(c_1 - \beta) + \alpha(\beta - \gamma)}$.

We have $\beta, \gamma \in [0, c_1]$, $\delta, \lambda \in [0, c_2]$ and $\alpha, \varepsilon \in [0, c_3]$. Therefore $0 \le \frac{c_2\gamma(c_3 - \alpha)}{c_3(c_1 - \beta) + \alpha(\beta - \gamma)} \le c_2$. The left inequality is satisfied if $c_3\beta + \alpha\gamma \le c_1 c_3 + \alpha\beta$ and the right inequality is satisfied if $c_3(\beta + \gamma) \le c_1 c_3 + \alpha\beta$. The second inequality implies the first one because $c_3\beta + \alpha\gamma \le c_3(\beta + \gamma)$ and $\alpha \le c_3$. We also have $0 \le \frac{\beta(c_3 - \alpha)}{c_1 - \gamma} \le c_3$. The left inequality is always satisfied and the right inequality is satisfied if $c_3(\beta + \gamma) \le c_1 c_3 + \alpha\beta$. We also have $0 \le \frac{c_2\alpha(c_1 - \gamma)}{c_3(c_1 - \beta) + \alpha(\beta - \gamma)} \le c_2$. The left inequality is satisfied if $c_3\beta + \alpha\gamma \le c_1 c_3 + \alpha\beta$ and the right inequality is always satisfied because $(c_1 - \beta)(c_3 - \alpha) \ge 0$. Therefore only one inequality stands:

$$\beta \le \frac{c_3(c_1 - \gamma)}{c_3 - \alpha}$$

We introduce three points $P_1 = (h_1, 0, 0)$, $P_2 = (0, h_2, 0)$, and $P_3 = (0, 0, h_3)$ where $h_1 = \frac{c_1 c_3 - \alpha\gamma}{c_3 - \alpha}$, $h_2 = \frac{c_2(c_1 c_3 - \alpha\gamma)}{c_3(c_1 - \beta) + \alpha(\beta - \gamma)}$, and $h_3 = \frac{c_1 c_3 - \alpha\gamma}{c_1 - \gamma}$. $P_1$ corresponds to the intersection of the planes $\{y = 0\}$ and $\{z = 0\}$ with the interface, $P_2$ corresponds to the intersection of the planes $\{x = 0\}$ and $\{z = 0\}$ with the interface

and $P_3$ corresponds to the intersection of the planes $\{x=0\}$ and $\{y=0\}$ with the interface. The volume and the centroid of the domain $AFO_1BEO_2DCO_3O$ are computed using the additivity of the volume and the first momentum of the tetrahedrons $OP_1P_2P_3$, $O_1AFP_1$, $O_2BEP_2$, and $O_3CDP_3$. Therefore, the volume is given by:

$$\mathcal{V}_{\mathrm{h}}(\alpha,\beta,\gamma) = \frac{c_2(c_3-\alpha)^2(c_1^3-\beta^3-\gamma^3)+3c_1c_2\alpha(c_1-\gamma)(c_1c_3-\alpha\gamma)}{6(c_1-\gamma)(c_3(c_1-\beta)+\alpha(\beta-\gamma))} \tag{C.35}$$

The centroid is given by:

$$\mathcal{C}_h(\alpha,\beta,\gamma) = \left[\begin{array}{c} \frac{(c_3-\alpha)^2(c_1^4-\beta^4-\gamma^4)+2c_1^2\alpha(c_1-\gamma)(2(c_1c_3-\alpha\gamma)+\alpha(c_1-\gamma))}{4((c_3-\alpha)^2(c_1^3-\beta^3-\gamma^3)+3c_1\alpha(c_1-\gamma)(c_1c_3-\alpha\gamma))} \\ \frac{c_2((c_3-\alpha)^3(c_1^4-\beta^4-\gamma^4)+2c_1\alpha(c_1-\gamma)(2(c_1c_3-\alpha\gamma)^2-c_1\alpha(c_3-\alpha)(c_1-\gamma))-4\beta^3(c_3-\alpha)^2(c_3(c_1-\beta)+\alpha(\beta-\gamma)))}{4(c_3(c_1-\beta)+\alpha(\beta-\gamma))((c_3-\alpha)^2(c_1^3-\beta^3-\gamma^3)+3c_1\alpha(c_1-\gamma)(c_1c_3-\alpha\gamma))} \\ \frac{(c_3-\alpha)^3(c_1^4-\beta^4-\gamma^4)+2c_1\alpha(c_1-\gamma)(2(c_1c_3-\alpha\gamma)^2-c_1\alpha(c_3-\alpha)(c_1-\gamma))-4\gamma^3(c_3-\alpha)^2(c_3(c_1-\gamma))}{4(c_1-\gamma)((c_3-\alpha)^2(c_1^3-\beta^3-\gamma^3)+3c_1\alpha(c_1-\gamma)(c_1c_3-\alpha\gamma))} \end{array}\right] \tag{C.36}$$

Note that the volume and the centroid are continuous between the `Penta` and the `Hexa` configurations since $\mathcal{V}_{\mathrm{h}}(0,\beta,\gamma) = \mathcal{V}_{\mathrm{p}}(c_1,\beta,\gamma)$ and $\mathcal{C}_{\mathrm{h}}(0,\beta,\gamma) = \mathcal{C}_{\mathrm{p}}(c_1,\beta,\gamma)$. By imposing a reference fixed volume $\mathcal{V}$ in (C.35), $\beta$ is the solution of the following third degree polynomial:

$$\Psi_{\mathrm{h}}(\alpha,\beta,\gamma) = \beta^3 - \frac{6\mathcal{V}(c_1-\gamma)}{c_2(c_3-\alpha)}\beta - \frac{(c_1-\gamma)}{c_2(c_3-\alpha)^2}\left(c_2(c_3-\alpha)^2(c_1^2+c_1\gamma+\gamma^2)+3(c_1c_3-\alpha\gamma)(c_1c_2\alpha-2\mathcal{V})\right)=0 \tag{C.37}$$

Let us find the definition domain of the `Hexa` configuration:

$$\mathcal{D}_h^{\mathcal{V}} = \left\{(\alpha,\gamma)\in[0,c_3]\times[0,c_1]\ \middle|\ 0\leq\beta_h(\alpha,\gamma,\mathcal{V})\leq c_1 \text{ and } \beta_h(\alpha,\gamma,\mathcal{V})\leq\frac{c_3(c_1-\gamma)}{c_3-\alpha}\right\}$$

where $\beta_h(\alpha,\gamma,\mathcal{V})$ is solution of equation (C.37). To find this domain, let use first find its boundaries. From equation (C.37), we have:

For $\beta=0$ $\qquad \Psi_{\mathrm{h}}(\alpha,0,\gamma) = -(c_1-\gamma)(\gamma-g_{\mathcal{V}}(\alpha))(\gamma-\tilde{g}_{\mathcal{V}}(\alpha)) = 0$

For $\beta=\dfrac{c_3(c_1-\gamma)}{c_3-\alpha}$ $\qquad \Psi_{\mathrm{h}}\left(\alpha,\dfrac{c_3(c_1-\gamma)}{c_3-\alpha},\gamma\right) = \dfrac{\alpha(c_1-\gamma)(\alpha^2+3c_3(c_3-\alpha))}{(c_3-\alpha)^3}(\gamma-h_{\mathcal{V}}^{13}(\alpha))(\gamma-\tilde{h}_{\mathcal{V}}^{13}(\alpha)) = 0$

For $\beta=c_1$ $\qquad \Psi_{\mathrm{h}}(\alpha,c_1,\gamma) = \dfrac{\gamma(\gamma^2+3c_1(c_1-\gamma))}{(c_3-\alpha)^2}(\alpha-h_{\mathcal{V}}^{31}(\gamma))(\alpha-\tilde{h}_{\mathcal{V}}^{31}(\gamma)) = 0$

where $\tilde{g}_{\mathcal{V}}$ and $\tilde{h}_{\mathcal{V}}^{13}$ are the conjugate roots of $g_{\mathcal{V}}$ and $h_{\mathcal{V}}$ defined in equation (C.5) and (C.6). These functions are well defined, but outside of the domain $[0,c_3]\times[0,c_1]$. Furthermore, $h_{\mathcal{V}}^{31}$ is the same function as $h_{\mathcal{V}}^{13}$ where $c_1$ and $c_3$ are swapped.

The possible limits of the domain $\mathcal{D}_h^{\mathcal{V}}$ are necessary in the following list: $\alpha=0$, $\alpha=c_3$, $\gamma=0$, $\gamma=c_1$, $\gamma=g_{\mathcal{V}}(\alpha)$, $\gamma=h_{\mathcal{V}}^{13}(\alpha)$, or $\alpha=h_{\mathcal{V}}^{31}(\gamma)$. These curves form a partition of the domain $[0,c_3]\times[0,c_1]$ in six regions such as presented in figure C.16. Thus $\mathcal{D}_h^{\mathcal{V}}$ is the reunion of some — possibly only one — of these regions. It is easy to check numerically by picking one value in these regions that three of these domains can not correspond since $\beta\notin\mathbb{R}$, $\beta\notin[0,c_1]$ or $\beta>\frac{c_3(c_1-\gamma)}{c_3-\alpha}$ in these domains. Therefore, the definition domain of the `Hexa` is necessarily given by:

$$\mathcal{D}_h^{\mathcal{V}} = \left\{(\alpha,\gamma)\in[0,c_3]\times[0,c_1]\ \middle|\ \gamma\leq g_{\mathcal{V}}(\alpha)\right\}$$

The limit curves are given by $\Gamma_{\mathrm{h}}^1:\gamma\mapsto(0,\gamma)$ where $\gamma\in[0,f_{\mathcal{V}}^{23}(c_1)]$, $\Gamma_{\mathrm{h}}^2:\alpha\mapsto(\alpha,g_{\mathcal{V}}(\alpha))$ where $\alpha\in[0,f_{\mathcal{V}}^{12}(c_3)]$ and $\Gamma_{\mathrm{h}}^3:\alpha\mapsto(\alpha,0)$ where $\alpha\in[0,f_{\mathcal{V}}^{12}(c_3)]$.

We can show that the discriminant of the third degree polynomial (C.37) is negative on $\mathcal{D}_{\mathrm{h}}^{\mathcal{V}}$ and the only root that verifies $0\leq\beta\leq c_1$ and $\beta\leq\frac{c_3(c_1-\gamma)}{c_3-\alpha}$ is given by:

$$\beta_{\mathrm{h}}(\alpha,\gamma,\mathcal{V}) = 2\sqrt{\frac{2\mathcal{V}(c_1-\gamma)}{c_2(c_3-\alpha)}}\cos\left(\frac{1}{3}\arccos\left(\frac{c_2(c_3-\alpha)^2(c_1^2+c_1\gamma+\gamma^2)+3(c_1c_3-\alpha\gamma)(c_1c_2\alpha-2\mathcal{V})}{4\mathcal{V}\sqrt{2\mathcal{V}(c_1-\gamma)(c_3-\alpha)/c_2}}\right)+\frac{4\pi}{3}\right) \tag{C.38}$$

The proof of this formula follows the same line as for the `Penta` configuration. The discriminant $\Delta_h$ can be seen as a third degree polynomial in the volume $\mathcal{V}$ instead of a fourth degree polynomial in $\alpha$ or $\gamma$ using a suitable change of the quantifiers. Then, we compute the roots of the derivative of $\Delta_h$ and show appropriate inequalities that prove the desired result. Afterwards, we use the proposition 1 with $\mathcal{K} = c_1$ and $\mathcal{K} = \frac{c_3(c_1-\gamma)}{c_3-\alpha}$ to prove that only the root $k = 2$ verifies $0 \leq \beta \leq c_1$ and $\beta \leq \frac{c_3(c_1-\gamma)}{c_3-\alpha}$. Nevertheless, the proof required the computation and the comparison of the curves $\{Y_h = \frac{1}{2}\}$ and $\{\Psi_h = 0\}$ because $\Psi_h$ is not of constant sign on $\mathcal{D}_h^{\mathcal{V}}$ like in the `Penta` case.

*Appendix C.6.2. Parametrization in $(\theta, \phi)$ of the centroid and the centroid in $(\theta, \phi)$*

From equations (C.3) and (C.34), we get $\tan(\theta) = \frac{c_3(c_1-\beta)+\alpha(\beta-\gamma)}{c_2(c_3-\alpha)}$ and $\cot(\phi) = \frac{c_1-\gamma}{c_3-\alpha}\cos(\theta)$. These equations are difficult to solve directly because of the expression of $\beta$ in (C.38). Instead, the trick is to express $\alpha$ and $\gamma$ with respect to $\beta$, $\theta$, and $\phi$ and to get a third degree polynomial on $\beta$ from the equation of the volume (C.35). We introduce the following notations:

$$\alpha = \frac{\beta - c_1 + T_2}{H_2} \qquad \gamma = \beta + T_2 - T_3 \qquad T_2 = c_2 \tan(\theta) \qquad T_3 = c_3 \cot(\phi)\sec(\theta) \qquad (C.39)$$

We replace these expressions in (C.35) to obtain the following third degree polynomial in $\beta$:

$$\left(\beta - \frac{1}{2}(c_1 - T_2 + T_3)\right)^3 - \frac{3}{4}T_4\left(\beta - \frac{1}{2}(c_1 - T_2 + T_3)\right) - \frac{3}{2}T_2 T_3(c_1 - \ell_{23}) = 0$$

where $T_4 = 4c_1 T_3 - (c_1 - T_2 + T_3)^2$. We already know that the three roots are real. Like for the `Penta` configuration, we can apply the extended proposition with $\mathcal{K} = 0$, $\mathcal{K} = c_1$, and $\mathcal{K} = \frac{c_3(c_1-\gamma)}{c_3-\alpha}$ to $\alpha$, $\beta$ and $\gamma$ and show that the only root that verifies $\beta \leq \frac{c_3(c_1-\gamma)}{c_3-\alpha}$, $0 \leq \alpha \leq c_1$, $0 \leq \beta \leq c_1$, and $0 \leq \gamma \leq c_1$ is given by the root $k = 2$:

$$\beta_h(\theta, \phi, \mathcal{V}) = \frac{1}{2}(c_1 - T_2 + T_3) + \sqrt{T_4}\mathcal{X}_h \qquad \mathcal{X}_h = \cos\left(\frac{1}{3}\arccos\left(\frac{6T_2 T_3(c_1 - \ell_{23})}{T_4^{\frac{3}{2}}}\right) + \frac{4\pi}{3}\right) \qquad (C.40)$$

where $c_1 \geq \ell_{23}$ and where $\mathcal{X}_h$ verifies the equation:

$$(\mathcal{X}_h)^3 - \frac{3}{4}\mathcal{X}_h - \frac{3T_2 T_3(c_1 - \ell_{23})}{2H_3^{\frac{3}{2}}} = 0 \qquad (C.41)$$

To obtain the final parametrization (20), we replace $\alpha$, $\beta$ and $\gamma$ in (C.36) by their expressions given in (C.39) and (C.40). We obtain a fourth degree polynomial in $\mathcal{X}_h$ for each component. Then we use equation (C.41) to get a second degree polynomial in each component. Finally, after some simplifications, we obtain equation (20).

*Appendix C.7. Technical lemmas*

*Appendix C.7.1. General inequality*

**Proposition 1.** *Let $\Psi(\beta) = \beta^3 + p\beta + q$ a third degree polynomial in $\beta$. If the discriminant $\Delta = 4p^3 + 27q^2 \leq 0$, which implies $p \leq 0$, the roots of $\Psi(\beta)$ are real and given by:*

$$\forall k \in [\![0, 2]\!] \quad \beta_k = 2\sqrt{-\frac{p}{3}}\cos\left(\frac{1}{3}\arccos\left(\frac{-q}{2\sqrt{\left(-\frac{p}{3}\right)^3}}\right) + \frac{2k\pi}{3}\right)$$

*Then, the sign of $\beta - \mathcal{K}$ is the same as $\cos(\frac{1}{3}\arccos(X) + \frac{2k\pi}{3}) - Y$ where $X = \frac{-q}{2\sqrt{(-p/3)^3}}$ and $Y = \frac{\mathcal{K}}{2\sqrt{-p/3}}$. Furthermore, suppose that $-1 \leq X \leq 0$. Then, the three roots verify $\beta_1 \leq 0$, $\beta_0, \beta_2 \geq 0$ and we have the following inequalities where $\Psi$ stands for $\Psi(\mathcal{K})$:*

| $Y \leq 0$ | $0 \leq Y \leq \frac{1}{2}$ | | $\frac{1}{2} \leq Y \leq 1$ | | $Y \geq 1$ |
|---|---|---|---|---|---|
| $\beta_0 \geq \mathcal{K}$ | $\beta_0 \geq \mathcal{K}$ | | if $\Psi \leq 0$ $\quad \beta_0 \geq \mathcal{K}$ <br> if $\Psi \geq 0$ $\quad \beta_0 \leq \mathcal{K}$ | | $\beta_0 \leq \mathcal{K}$ |
| $\beta_2 \geq \mathcal{K}$ | if $\Psi \leq 0$ | $\beta_2 \leq \mathcal{K}$ | $\beta_2 \leq \mathcal{K}$ | | $\beta_2 \leq \mathcal{K}$ |
| | if $\Psi \geq 0$ | $\beta_2 \geq \mathcal{K}$ | | | |

*Proof.* We have the following identities for $x \in [0, 2\pi]$:

$$\cos\big(\arccos(x)\big) = x \qquad \arccos\big(\cos(x)\big) = \begin{cases} x & \text{if} \quad 0 \leq x \leq \pi \\ 2\pi - x & \text{if} \quad \pi < x < 2\pi \end{cases} \tag{C.42}$$

It is easy to check that:

$$X - \cos\big(3\arccos(Y)\big) = X - (4Y^3 - 3Y) = -\frac{\Psi(\mathcal{K})}{2\sqrt{(-p/3)^3}} \tag{C.43}$$

We have the inequalities $(4k+1)\frac{\pi}{6} \leq \frac{1}{3}(\arccos(X)+2k\pi) \leq (4k+2)\frac{\pi}{6}$, so $\beta_1 \leq 0$ and $\beta_0, \beta_2 \geq 0$. In the first part of the proof, we use only the hypothesis $-1 \leq X \leq 0$ and not the expression of $X$ and $Y$. If $0 \leq Y \leq \frac{1}{2}$, we have $\frac{\pi}{6} \leq \frac{1}{3}(\arccos(X)) \leq \frac{\pi}{3} \leq \arccos(Y) \leq \frac{\pi}{2}$. Since the cosine function is monotonically decreasing on $\left[\frac{\pi}{6}, \frac{\pi}{2}\right]$, we get by composition $\beta_0 \geq \mathcal{K}$. If $\frac{1}{2} \leq Y \leq 1$, we have $-\frac{\pi}{2} \leq \frac{1}{3}(\arccos(X) - 2\pi) \leq -\frac{\pi}{3} \leq -\arccos(Y) \leq 0$. Since the cosine function is monotonically increasing on $\left[-\frac{\pi}{2}, 0\right]$ we get by composition $\beta_2 \leq \mathcal{K}$. In the second part of the proof, we will use the identity (C.43). First, we suppose that $\Psi \leq 0$. Since arccos is monotonically decreasing, using (C.43), we get $\arccos(X) \leq \arccos(\cos(3\arccos(Y)))$. If $\frac{1}{2} \leq Y \leq 1$, from (C.42), we get $\arccos(X) \leq 3\arccos(Y)$, so $\frac{\pi}{6} \leq \frac{1}{3}\arccos(X) \leq \arccos(Y) \leq \frac{\pi}{3}$. Since the cosine function is monotonically decreasing on $\left[\frac{\pi}{6}, \frac{\pi}{3}\right]$, we get $\beta_0 \geq \mathcal{K}$. If $0 \leq Y \leq 1/2$, from (C.42), we get $\arccos(X) \leq 2\pi - 3\arccos(Y)$, so $\frac{\pi}{3} \leq \arccos(Y) \leq \frac{1}{3}(2\pi - \arccos(X)) \leq \frac{\pi}{2}$. Since the cosine function is monotonically decreasing on $\left[\frac{\pi}{3}, \frac{\pi}{2}\right]$, we get $\beta_2 \leq \mathcal{K}$. If $\Psi \geq 0$, the proof is the same but the inequalities are reversed because of (C.43). $\qquad \square$

*Appendix C.7.2. Analytical expression for the* `Penta` *configuration of* $\beta_{\mathrm{p}}$ *on* $\mathcal{D}_{\mathrm{p}}^{\mathcal{V}}$

We want to find an analytical expression of $\beta$ that verifies $0 \leq \beta \leq \alpha - \gamma$ on $\mathcal{D}_{\mathrm{p}}^{\mathcal{V}}$. The discriminant of the third degree polynomial (C.22) is given by $\Delta = 27(\alpha - \gamma)^2 \Delta_p$ where:

$$\Delta_p(\alpha, \gamma, \ell_{23}) = \big(\alpha^2 + \alpha\gamma + \gamma^2 - 3\ell_{23}\alpha\big)^2 - 4(\alpha - \gamma)(\ell_{23})^3$$

First, let us show that $\Delta_p$ is negative on the definition domain of the `Penta` $\mathcal{D}_{\mathrm{p}}^{\mathcal{V}}$ which writes:

$$\forall c_1 > 0, \quad \forall \ell_{23} \in [0, c_1], \quad \forall \alpha \in [\ell_{23}, \min(c_1, 3\ell_{23})], \quad \forall \gamma \in [0, f_{\mathcal{V}}^{23}(\alpha)], \quad \Delta_p(\alpha, \gamma, \ell_{23}) \leq 0$$

This expression is a fourth degree polynomial in $\alpha$ and $\gamma$. To prove that $\Delta_p$ is negative appears to be a complicated task. Instead we can see $\Delta_p$ as a third degree polynomial in $\ell_{23}$. As illustrated in figure C.17, it is equivalent to show that:

$$\forall c_1 > 0, \quad \forall \alpha \in [0, c_1], \quad \forall \gamma \in [0, \alpha], \quad \forall \ell_{23} \in [\ell_{23}^{\min}(\alpha, \gamma), \ell_{23}^{\max}(\alpha, \gamma)], \quad \Delta_p(\alpha, \gamma, \ell_{23}) \leq 0 \tag{C.44}$$

where $\ell_{23}^{\min}(\alpha, \gamma) = \frac{\alpha^2 + \alpha\gamma + \gamma^2}{3\alpha}$ and $\ell_{23}^{\max}(\alpha, \gamma) = \alpha$.
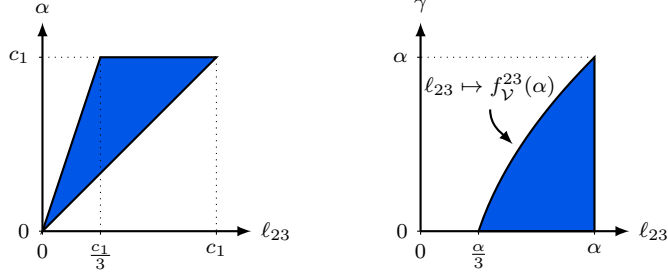
Figure C.17: Illustration of the inversion of the quantifiers.

The partial derivative of $\Delta_p$ with respect to $\ell_{23}$ writes:

$$\frac{\partial \Delta_p}{\partial \ell_{23}} = -6\big(2(\alpha - \gamma)(\ell_{23})^2 - 3\alpha^2 \ell_{23} + \alpha(\alpha^2 + \alpha\gamma + \gamma^2)\big)$$

The roots of second degree polynomial $\frac{\partial \Delta_p}{\partial \ell_{23}}$ are given by $\ell_{23}^{\pm}(\alpha, \gamma) = \frac{3\alpha^2 \pm \sqrt{\alpha^4 + 8\alpha\gamma^3}}{4(\alpha - \gamma)}$. We have the following inequalities:

$$\ell_{23}^{\min}(\alpha, \gamma) \leq \ell_{23}^{-}(\alpha, \gamma) \leq \ell_{23}^{\max}(\alpha, \gamma) \leq \ell_{23}^{+}(\alpha, \gamma) \tag{C.45}$$

The right and the middle inequalities are equivalent to $8\alpha\gamma(\alpha - \gamma)^2 \geq 0$. The left one is equivalent to $16(\alpha^3 - \gamma^3)^2 \geq 0$. We also have:

$$\Delta_p\left(\alpha, \gamma, \ell_{23}^{\min}(\alpha, \gamma)\right) = -4(\alpha - \gamma)\left(\ell_{23}^{\min}(\alpha, \gamma)\right)^3 \leq 0 \quad \Delta_p(\alpha, \gamma, \ell_{23}^{\max}(\alpha, \gamma)) = -(\alpha - \gamma)(3\alpha + \gamma)\gamma^2 \leq 0 \tag{C.46}$$

The second degree polynomial $\frac{\partial \Delta_p}{\partial \ell_{23}}$ is positive on the interval $[\ell_{23}^{-}, \ell_{23}^{+}]$ and negative outside. Hence $\ell_{23} \mapsto \Delta_p(\alpha, \gamma, \ell_{23})$ is monotonically increasing on $[\ell_{23}^{-}, \ell_{23}^{+}]$ and monotonically decreasing elsewhere. Therefore, together with (C.46) and the inequalities (C.45), we get equation (C.44). The three solutions of (C.22) are then real and given by:

$$\tilde{\beta}_k = 2\sqrt{\ell_{23}(\alpha - \gamma)} \cos\left(\frac{1}{3}\arccos\left(X_{\mathrm{p}}\right) + \frac{2k\pi}{3}\right) \qquad X_{\mathrm{p}} = \frac{\alpha^2 + \alpha\gamma + \gamma^2 - 3\ell_{23}\alpha}{2\ell_{23}\sqrt{\ell_{23}(\alpha - \gamma)}}$$

where $k \in \{0, 1, 2\}$. Now, let us show that the root $k = 2$ is the only one which verifies $0 \leq \tilde{\beta}_2 \leq \alpha - \gamma$. We introduce $\mathcal{K} = \alpha - \gamma$ and the notations:

$$Y_{\mathrm{p}} = \frac{\alpha - \gamma}{2\sqrt{\ell_{23}(\alpha - \gamma)}} = \sqrt{\frac{\alpha - \gamma}{4\ell_{23}}}$$

On $\mathcal{D}_{\mathrm{p}}^{\mathcal{V}}$, we have $-1 \leq X_{\mathrm{p}} \leq 0$ — since $\Delta_p \leq 0$ — and $0 \leq Y_{\mathrm{p}} \leq \frac{\sqrt{3}}{2} \leq 1$ since $\gamma \geq \alpha - 3\ell_{23}$. We also have:

$$\Psi_{\mathrm{p}}(\alpha, \alpha - \gamma, \gamma) = 3\gamma(\alpha - \gamma)(\ell_{23} - \alpha) \leq 0$$

Using the proposition 1, we get $\tilde{\beta}_0 \geq \alpha - \gamma$, $\tilde{\beta}_1 \leq 0$, and $\tilde{\beta}_2 \leq \alpha - \gamma$. Therefore, we obtain the formula of the `Penta` configuration (C.25).

## References

[1] F. Gibou, R. Fedkiw, S. Osher, A review of level-set methods and some recent applications, Journal of Computational Physics 353 (2018) 82–109 (2018).

[2] G. Tryggvason, B. Bunner, A. Esmaeeli, D. Juric, N. Al-Rawahi, W. Tauber, J. Han, S. Nas, Y.-J. Jan, A front-tracking method for the computations of multiphase flow, Journal of computational physics 169 (2) (2001) 708–759 (2001).

[3] V. Dyadechko, M. Shashkov, Moment-of-fluid interface reconstruction, Los Alamos National Laborator Report LA-UR-05-7571 (2005).

[4] V. Dyadechko, M. Shashkov, Moment-of-fluid interface reconstruction, Los Alamos National Laborator Report LA-UR-07-1537 (2007).

[5] H. T. Ahn, M. Shashkov, Multi-material interface reconstruction on generalized polyhedral meshes, Journal of Computational Physics 226 (2) (2007) 2096–2132 (2007).

[6] V. Dyadechko, M. Shashkov, Reconstruction of multi-material interfaces from moment data, Journal of Computational Physics 227 (11) (2008) 5361–5384 (2008).

[7] H. T. Ahn, M. Shashkov, Adaptive moment-of-fluid method, Journal of Computational Physics 228 (8) (2009) 2792–2821 (2009).

[8] H. Anbarlooei, K. Mazaheri, 'moment of fluid'interface reconstruction method in axisymmetric coordinates, International Journal for Numerical Methods in Biomedical Engineering 27 (10) (2011) 1640–1651 (2011).

[9] S. Galera, J. Breil, P.-H. Maire, A 2d unstructured multi-material cell-centered arbitrary lagrangian–eulerian (ccale) scheme using mof interface reconstruction, Computers & Fluids 46 (1) (2011) 237–244 (2011).

[10] S. P. Schofield, M. A. Christon, Effects of element order and interface reconstruction in fem/volume-of-fluid incompressible flow simulation, International Journal for Numerical Methods in Fluids 68 (11) (2012) 1422–1437 (2012).

[11] J. Breil, T. Harribey, P.-H. Maire, M. Shashkov, A multi-material reale method with mof interface reconstruction, Computers & Fluids 83 (2013) 115–125 (2013).

[12] M. Jemison, E. Loch, M. Sussman, M. Shashkov, M. Arienti, M. Ohta, Y. Wang, A coupled level set-moment of fluid method for incompressible two-phase flows, Journal of Scientific Computing 54 (2-3) (2013) 454–491 (2013).

[13] R. N. Hill, M. Shashkov, The symmetric moment-of-fluid interface reconstruction algorithm, Journal of Computational Physics 249 (2013) 180–184 (2013).

[14] M. B. Friess, J. Breil, P.-H. Maire, M. Shashkov, A multi-material ccale-mof approach in cylindrical geometry, Communications in Computational Physics 15 (2) (2014) 330–364 (2014).

[15] M. Jemison, M. Sussman, M. Arienti, Compressible, multiphase semi-implicit method with moment of fluid interface representation, Journal of Computational Physics 279 (2014) 182–217 (2014).

[16] M. Jemison, M. Sussman, M. Shashkov, Filament capturing with the multimaterial moment-of-fluid method, Journal of Computational Physics 285 (2015) 149–172 (2015).

[17] X. Chen, X. Zhang, An improved 3d mof method based on analytical partial derivatives, Journal of Computational Physics 326 (2016) 156–170 (2016).

[18] A. Lemoine, S. Glockner, J. Breil, Moment-of-fluid analytic reconstruction on 2d cartesian grids, Journal of Computational Physics 328 (2017) 131–139 (2017).

[19] X. Chen, X. Zhang, An improved 2d mof method by using high order derivatives, Journal of Computational Physics 349 (2017) 176–190 (2017).

[20] E. Kikinzon, M. Shashkov, R. Garimella, Establishing mesh topology in multi-material cells: enabling technology for robust and accurate multi-material simulations, Computers & Fluids (2018).

[21] A. Asuri Mukundan, T. Ménard, A. Berlemont, J. C. B. de Motta, Interface reconstruction method for multiphase flows in under-resolved regions, in: International Conference on Computational Fluid Dynamics, 2018, pp. 1–17 (Jul 2018).
URL http://www.iccfd.org/iccfd10/papers/ICCFD10-013-Paper.pdf

[22] F. Qing, X. Yu, Z. Jia, A robust mof method applicable to severely deformed polygonal mesh, Journal of Computational Physics 377 (2019) 162–182 (2019).

[23] W. J. Rider, D. B. Kothe, Reconstructing volume tracking, Journal of computational physics 141 (2) (1998) 112–152 (1998).

[24] S. Diot, M. M. François, An interface reconstruction method based on an analytical formula for 3d arbitrary convex cells, Journal of Computational Physics 305 (2016) 63–74 (2016).

[25] R. Nürnberg, Calculating the area and centroid of a polygon in 2d (2013).
URL http://www.ma.ic.ac.uk/~rn/centroid.pdf

[26] Notus website, https://notus-cfd.org (2019).

[27] M. Coquerelle, S. Glockner, A fourth-order accurate curvature computation in a level set framework for two-phase flows subjected to surface tension forces, Journal of Computational Physics 305 (2016) 838–876 (2016).

[28] J. Picot, S. Glockner, Reduction of the discretization stencil of direct forcing immersed boundary methods on rectangular cells: The ghost node shifting method, Journal of Computational Physics 364 (2018) 18 − 48 (2018). doi:https://doi.org/10.1016/j.jcp.2018.02.047.
URL http://www.sciencedirect.com/science/article/pii/S0021999118301360

[29] R. Swinbank, R. J. Purser, Fibonacci grids: A novel approach to global modelling, Quarterly Journal of the Royal Meteorological Society 132 (619) (2006) 1769–1793 (2006).

[30] R. Fletcher, Practical methods of optimization, John Wiley & Sons, 1987 (1987).